A refinement indicator for adaptive quasicontinuum approaches for structural lattices

Li Chen[a,b], Péter Z. Berke[a], Thierry J. Massart[a],
Lars A.A. Beex[b], Marco Magliulo[b], Stéphane P.A. Bordas[c,b,d]

[a] Building Architecture and Town Planning Department
Université Libre de Bruxelles (ULB)
Avenue F.D. Roosevelt 50, 1050 Brussels, Belgium

[b] Department of Engineering, Institute of Computational Engineering
University of Luxembourg
Maison du Nombre, 6 Avenue de la Fonte, 4364 Esch-sur-Alzette,
Luxembourg

[c] Institute of Research and Development
Duy Tan University
K7/25 Quang Trung, Danang, Vietnam.

[d] Department of Medical Research, China Medical University Hospital
China Medical University
Taichung, Taiwan

Abstract

The quasicontinuum method is a concurrent multiscale approach in which lattice models are fully resolved in small regions of interest and coarse-grained elsewhere. Since the method was originally proposed to accelerate atomistic lattice simulations, its refinement criteria – that drive refining coarse-grained regions and/or increasing fully-resolved regions – are generally associated with quantities relevant to the atomistic scale. In this contribution, a new refinement indicator is presented, based on the energies of dedicated cells at coarse-grained domain surfaces. This indicator is incorporated in an adaptive scheme of a generalization of the quasicontinuum method able to consider periodic representative volume elements, like the ones employed in most computational homogenization approaches. However, this indicator can also be used for conventional quasicontinuum frameworks. Illustrative numerical examples of elastic indentation and scratch of different lattices demonstrate the capabilities of the refinement indicator and its impact on adaptive quasicontinuum simulations.

Keyword:

generalized quasicontinuum method

adaptivity

refinement indicator

3D co-rotational beam

structural lattices

1 Introduction

The quasicontinuum (QC) method is a concurrent multiscale approach that aims to decrease the computational costs of mesostructural, microstructural or nanostructural lattice models. The approach fully resolves the lattice model in small regions of interest (fully-resolved domains: FRDs), whereas in the remainder of the domain the degrees of freedom (DoFs) of the lattice model are interpolated (coarse-grained domains: CGDs). The CGDs are subdivided into non-overlapping interpolation elements (IPEs), inside each of which the shape functions of finite elements are used to interpolate the DoFs. As the interpolation decreases the number of DoFs, the efforts to *solve* the governing equations are significantly reduced. A second reduction step, often called summation or sampling, is necessary to decrease the efforts to *construct* the governing equations. Summation in QC terminology means that only a few lattice interactions are sampled to approximate the contributions of all lattice interactions in the CGDs to the governing equations.

The QC method was originally proposed to decrease the computational expenses of atomistic lattices simulation - characterized by conservative interactions [2, 21, 22, 26, 27, 35, 36, 44, 45, 47, 50]. Later, it was reformulated by Beex et al. [8–10] using a virtual-power-statement to incorporate dissipative phenomena. Kochmann and Amelang [22], Rokoš et al. [39–41] have demonstrated that dissipation can also be incorporated using variational statements. These reformulations have widened the method's applicability to lattice models of discrete and fibrous materials in which each yarn, fiber or strut is represented using a series of consecutive springs or beams.

Another enhancement was recently proposed by Mikeš et al. [31–34], who have made the approach applicable to geometrically irregular lattices – albeit the mechanical behaviour of each interaction is the same. A disadvantage of

this approach is that summation cannot truly be exploited to decrease the construction of the governing equations because each interaction is evaluated to get a homogenized material tensor. The approach was recently used by Ghareeb and Elbanna [19] to investigate networks of polymer chains.

Traditionally, the interpolation in the CGDs is performed indiscriminately: the DoFs of all lattice nodes are interpolated in the same manner – without regarding the connectivity pattern of the lattice. Consequently, the QC method is traditionally only exploited for regular lattices, where each lattice node is connected to its neighbouring lattice nodes in the same manner (or single Bravais lattice in atomstics terminology [14]).

Recently however, Chen et al. [13] and Phlipot and Kochmann [38] have proposed generalization in which a more complex connectivity of the lattice is considered (or multi-lattice in atomistics terminology [14]). As a result, the method can also be applied to more complex lattice models, in which each lattice node inside a periodic unit cell is connected to its neighboring nodes in different patterns – using interactions of which the mechanical response can vary. Consequently, this particular QC framework can be used for any type of micro-structural model, as long as its micro-structural arrangement is periodic.

The generalization is based on interpolating the DoFs of each lattice node in a periodic unit cell (i.e. the smallest repeating geometrically similar units in a periodic lattice) individually. Thus, a disadvantage of the generalization is that many more DoFs remain - relative to the macro-models of computational homogenization (FE^2) approaches [12, 18, 20, 29]. Another disadvantage is that more unit cells must be sampled inside each IPE. Advantages over nested approaches based on computational homogenization are that: (i) macro-to-micro and micro-to-macro relations are avoided, (ii) no micro-structural boundary conditions are necessary, and (iii) scale-separation does not need to hold.

Adaptivity of QC approaches is mainly investigated in the context of atomistic lattices for metals [24, 30, 34, 36, 46]. Error estimators were proposed from a mathematical point of view for the force based atomistic QC by Dobson et al. [15], Arndt and Luskin [1] and for the energy based atomistic QC by Wang [48], Ortner and Wang [37]. For this reason, most of the refinement indicators in the realm of structural lattices are based on quantities that are relevant for regular atomistic lattices and metals [24,34,36,46]. For instance, Phlipot and Kochmann [38] have used a refinement indicator based on the (continuum derived) J_2 invariant of the deformation, even though their meso-structural lattice represents a discrete multi-lattice [14]. A disadvantage of this indicator is that refinement may also be triggered for homogeneous deformations and rigid body rotations. Note that structural lattices and atomistic lattices are distinctive when applying QC. In structural lattices, nearest interactions such as trusses and beams are considered. In atomistic lattices, next to nearest interactions such as atomic potential are also incorporated.

To the best of the authors' knowledge, three studies have presented quite different refinement indicators for QC methods that are promising for structural lattices. First, Memarnahavandi et al. [30] have presented a goal-oriented adaptive QC approach in which not only the triangulation of IPEs (triangular shapes and corresponding finite element shape functions are used to interpolate the DoFs) was adapted, but also the size of the clusters of summation/sampling interactions. The disadvantage of this approach is that the cluster QC method is known to be relatively inaccurate [5–7, 7–11, 41], even if many sampling interactions are used.

Second, Rokoš et al. [40, 41] have presented adaptive QC formulations for damageable lattices, where the evolution of FRDs and CGDs was triggered by the development of damage in the lattice interactions. This indicator thus is only applicable to damageable lattices, and such a approach thus only triggers

refinement in regions where damage occurs, whereas refinement in other regions may also improve the accuracy for complex stress distributions – regardless of the occurrence of damage.

Third, Mikeš et al. [34] have formulated adaptivity based on the Zienkiewicz-Zhu indicator. The resulting adaptive scheme appears to be generally applicable and does not suffer from any of the drawbacks. A disadvantage for its use in the generalized variant of the QC method, which effectively superimposes as many finite element shape functions as classes of lattice nodes present in the lattice, is that no macroscopic deformation gradient can be recognized. One possibility would therefore be to combine the Zienkiewicz-Zhu indicator of Mikeš et al. [34] with the approach of Phlipot and Kochmann [38] in which as many macroscale deformation gradient tensors are distinguished as classes of lattice nodes are present.

Instead, the present contribution proposes a completely different refinement indicator that can be applied to both conventional QC methods as well as to its generalized variant (although we only demonstrate its use for the generalized variant here) in the realm of structural lattice. The core idea behind the new refinement indicator is placing a signaling cell on the edges of interpolation elements and measuring quantities of interest may be an applicable approach to other new types of refinement indicators including dissipation for instance. The need for refinement is indicated by placing a 'signaling' cell on each communicating IPE surface, and by determining two stored energies for each signaling cell: first by governing the signaling cell's deformation according to the first IPE, and second by governing the signaling cell's deformation according to the second IPE (i.e. the neighboring IPE that shares the same external surface). If the difference between the signaling cell's energies reaches a user-defined threshold, both IPEs are refined. At the periphery of the FRDs, some additional technicalities

must be incorporated, but the approach effectively remains the same.

If the volume of a newly created IPE reaches a user-defined minimum, it will be replaced by an FRD. This automatically increases the size of FRDs, but also enables FRDs to be created independently out of a cluster of IPEs (as the illustration results will reveal).

As mentioned before, the resulting adaptive scheme is demonstrated here for the generalized QC method, but because conventional QC methods are a subset of the generalized QC framework, the refinement indicator is also applicable for conventional QC approaches. The indicator's capabilities are demonstrated for 3D structures consisting of body-centered-cubic (BCC) and Kelvin cells of linear elastic, geometrically non-linear co-rotational beams. Within the cell, each strut is discretized with several beam elements, which are given independent geometrical and material parameters.

The remainder of this work is organized as follows. Section 2 outlines the generalized QC method. Section 3 presents the adaptive scheme including the detailed implementation of the refinement indicator. Section 4 illustrates the adaptive generalized QC method using numerical examples. Section 5 concludes the presented work.

2 Generalized QC method

For demonstration purposes, we explain the generalized QC method for the periodic cell in Fig. 1. However, it is emphasized that the approach is applicable to any type of cell, as long as it is periodic.

For the sake of a simple illustration let us consider the structural lattice of Fig. 2, which consists of an X shaped 2D cell of Fig. 1. The cell of Fig. 1 consists of four diagonal struts. Each strut is represented by a series of three beam elements. Each central beam element is given different geometrical and material

parameters than the outer ones – as presented by the blue and green colors. Beam finite elements [3] are used as structural models in the computation.

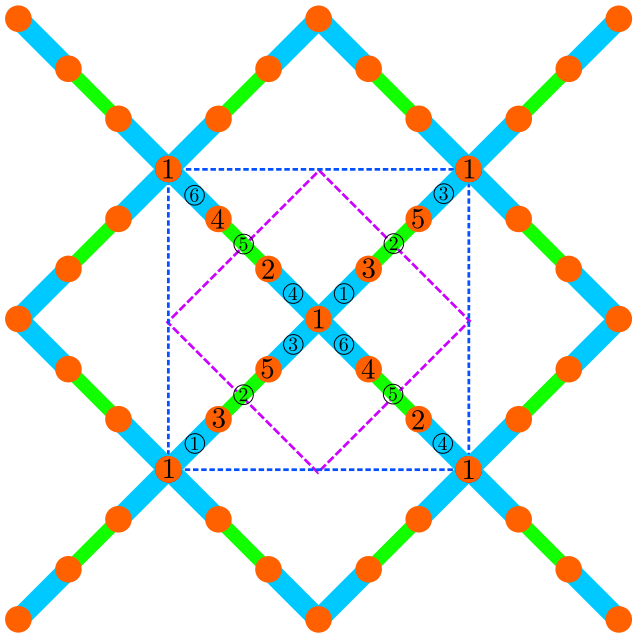

Figure 1: Beam representation of a 2D lattice that consists of X shaped cells. All blue beams are given the same geometrical and material parameters and the green beams are given their own geometrical and material parameters. Beam node types are indicated as $1-5$. Beam types are indicated as ① $-$ ⑥. The purple dash box marks a unit cell (i.e. the smallest repeating cell in a periodic lattice). The blue dash box marks the range of a sampling and signaling cell as is adopted in the presented work.

Notably, the authors distinguish between 'cell' and 'unit cell'. The term 'unit cell' refers to the smallest repetitive cell of a periodic lattice, while term 'cell' in the present work only needs to be periodic and might contain more than one unit cells. As for the illustrative lattice of Fig. 1, the range of a 'cell' and a 'unit cell' are indicated using dash boxes of different colors. In Fig. 1, as in the rest of the contribution, a 'cell' consists of two 'unit cells'.

We are interested in systems of large numbers of cells, because those typically appear in engineering applications. However, they are computationally

demanding because of the large number of DoFs.

As we restrict ourselves to (non-linear) elastic systems, the system can be *solved* by the following equations using Newton's method:

$$\delta\mathbf{u}^T(\mathbf{f}_{\text{int}}(\mathbf{u}^*) + \mathbf{K}(\mathbf{u}^*)d\mathbf{u}) = \delta\mathbf{u}^T\mathbf{f}_{\text{ext}} \tag{1}$$

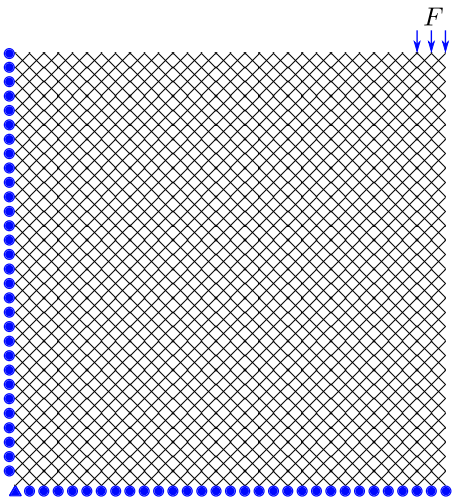

Figure 2: Two dimensional sketch of a large system of X-shaped cells.

In Eq. (1), $\mathbf{u}$ and $\mathbf{f}_{\text{ext}}$ denote the column matrices of the beam nodes *DoFs* and *external forces* (including moments), respectively. $\mathbf{u}^*$ and $d\mathbf{u}$ represent the estimation and the correction of $\mathbf{u}$. $\mathbf{f}_{\text{int}}(\mathbf{u})$ denotes the column of internal forces and is obtained as:

$$\mathbf{f}_{\text{int}}(\mathbf{u}) = \sum_{i=1}^{m} \frac{\partial E_i(\mathbf{u})}{\partial \mathbf{u}} \tag{2}$$

where $E_i(\mathbf{u})$ denotes the elastic strain energy of beam i and m denotes the total number of beam FEs. $\mathbf{K}(\mathbf{u})$ denotes the tangential stiffness matrix and is obtained as:

$$\mathbf{K}(\mathbf{u}) = \sum_{i=1}^{m} \frac{\partial^2 E_i(\mathbf{u})}{\partial \mathbf{u}^2} \tag{3}$$

Eq. (1) is referred to as the direct numerical simulation (DNS).

QC methods were proposed in order to decrease the computational costs of DNS, while keeping a reasonable accuracy. The method incorporates two model reduction steps: *interpolation* and *summation*.

2.1 Interpolation in the generalized QC method

The *interpolation* step of the generalized QC method divides the system into non-overlapping fully resolved-domains (FRDs) and coarse-grained domains (CGDs).

In the FRDs, the micro-structural beam representation is preserved. FRDs are typically restricted to small subdomains in which localized responses occur (e.g. strain localization and beam failures).

On the other hand, CGDs are employed in the remainder of the model domain in which the deformation fluctuations are substantially less local. The CGDs are further divided into interpolation elements (IPEs) to apply an interpolation of kinematics within each IPE (although any type of interpolation technique may of course be used, see e.g. [23]). The DoFs of all beam nodes in the IPEs are interpolated using FE shape functions and the representative DoFs defined at the nodes of the IPEs (same number and nature of DoFs as for a single beam node for each node type convoluted in an IPE nodal vector).

Fig. 3 illustrates a possible interpolation scheme for the system of Fig. 2, where the region near the external force is fully resolved and the remainder is coarse grained using linear triangular interpolation.

As a result of *interpolation*, only the DoFs of the beam nodes in the FRDs and of the *nodes of the IPEs* are preserved in the governing equations. This leads to a reduced set of DoFs (denoted as $\mathbf{u}_r$) and decreases the number of

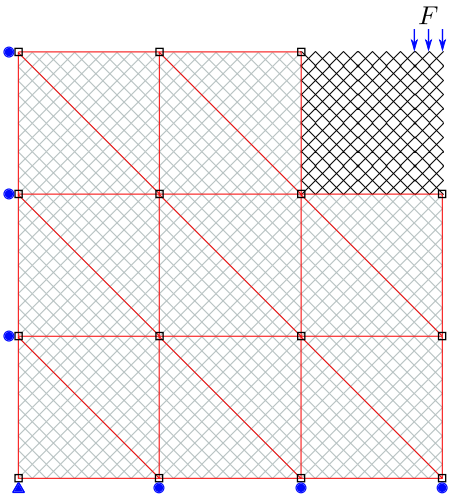

Figure 3: Illustration of interpolation in QC methods. □ denote the nodes of the IPEs.

governing equations and hence, the number of DoFs to solve for. $\mathbf{u}_r$ is related to the DoFs of all beam nodes, $\mathbf{u}$, using the condensation matrix $\mathbf{N}$, i.e.

$$\mathbf{u} = \mathbf{N}\mathbf{u}_r. \tag{4}$$

Consequently, Eq. (1) is revised as

$$\delta\mathbf{u}_r^T(\mathbf{N}^T\mathbf{f}_{\text{int}}(\mathbf{N}\mathbf{u}_r^*) + \mathbf{N}^T\mathbf{K}(\mathbf{N}\mathbf{u}_r^*)\mathbf{N}) = \delta\mathbf{u}_r^T\mathbf{N}^T\mathbf{f}_{\text{ext}} \tag{5}$$

with $\mathbf{u}_r^*$ denoting an estimation of $\mathbf{u}_r$ and $d\mathbf{u}_r$ the correction of $\mathbf{u}_r$.

Essential to realize is that the beam nodes in the cell of Fig. 1 are connected to their neighboring beam nodes in different ways. As a distinctive character, the *generalized* QC method [13] classifies the beam nodes of a cell into different types - based on their connectivity, which is identical to the decomposition of multi-lattice into several single Bravais lattices in the realm of atomistics [14, 38]. The DoFs of each type of beam node are interpolated independently. To facilitate

this, the nodes of the IPEs store multiple sets of DoFs – one set per type of beam node. These are used to independently interpolate the DoFs of the corresponding type of beam nodes.

For the cell of Fig. 1 for instance, a total of 13 beam nodes and 12 beam elements are present in a cell. The nodes in the cell are classified into 5 types according to the rule of decomposing multi-lattice into several single Bravais lattices [14, 38]. Moreover, differentiated by the beam node types of both ends, the 12 beam elements are categorized in 6 types. The beam type classification will play a role in the adaptivity scheme of Section 3.

2.2 Summation in the generalized QC method

The *summation* step of the QC methods aims to reduce the cost of the *construction* of the governing equations, by approximating the governing equations using much less beam elements, which are referred to as *sampling beams*. Each sampling beam is associated with a weight factor, which indicates the number of beams it represents. Consequently, $\mathbf{f}_{\text{int}}$ and $\mathbf{K}$ of Eqs. (2) and (3) are approximated as follows:

$$\bar{\mathbf{f}}_{\text{int}}(\mathbf{u}_s) = \sum_{i \in S} \omega_i \frac{\partial E_i(\mathbf{u}_s)}{\partial \mathbf{u}_s} \tag{6}$$

$$\bar{\mathbf{K}}(\mathbf{u}_s) = \sum_{i \in S} \omega_i \frac{\partial^2 E_i(\mathbf{u}_s)}{\partial \mathbf{u}_s^2} \tag{7}$$

where S denotes the set of sampling beams. ω_i denotes the weight of sampling beam i. $\mathbf{u}_s$ represents the column matrix that stores the kinematic variables of the nodes of the sampling beams. Note that $\mathbf{u}_s$ can be interpolated from $\mathbf{u}_r$ using the condensation matrix $\mathbf{N}_s$,

$$\mathbf{u}_s = \mathbf{N}_s \mathbf{u}_r. \tag{8}$$

After *summation*, Eq. (5) is revised as

$$\delta \mathbf{u}_r^T (\mathbf{N}_s^T \bar{\mathbf{f}}_{\text{int}}(\mathbf{N}_s \mathbf{u}_r^*) + \mathbf{N}_s^T \bar{\mathbf{K}}(\mathbf{N}_s \mathbf{u}_r^*) \mathbf{N}_s) = \delta \mathbf{u}_r^T \mathbf{N}^T \mathbf{f}_{\text{ext}} \tag{9}$$

The selection of the sampling beams proposed by Chen et al. [13] is used here and can be summarized as follows.

First, all beam elements that are either partially or completely inside FRDs are selected as *sampling beams*. Their weight factors are set to 1, since they only represent themselves. Since it is possible that the FRD-CGD interface cuts through the lattice, there are beams that are sectioned and these beams are by definition sampling beams of FRDs.

Second, in CGDs, a sufficient number of Gauss quadrature points (GQPs) are selected inside each IPE. A cell is centered at each GQP (which entails that the center of the cell does not necessarily match a center of a cell of the underlying system). The beam elements of these cells are also selected as sampling beams. The weight factors of these sampling beams are determined as

$$\omega = \mathrm{W}_{\mathrm{GQP}}^j \cdot \frac{V_{\mathrm{IPE}}}{V_{\mathrm{UC}}}, \qquad \text{with} \sum_{j=1}^{n_{\mathrm{GQP}}} \mathrm{W}_{\mathrm{GQP}}^j = 1, \tag{10}$$

where V_{IPE} and V_{UC} denote the volume of the IPE and the volume of a single cell, respectively. $\mathrm{W}_{\mathrm{GQP}}^j$ denotes the normalized weight of Gauss quadrature point (GQP) j and n_{GQP} denotes the number of GQPs.

An illustration of *summation* is presented in Fig. 4, where three GQPs are used per IPE. Note that the sufficient number of GQPs refers to the minimum number of GQPs to guarantee convergence.

For the summation, the number of sampling beams in CGDs can be minimized if a 'sampling cell' matches a 'unit cell'.

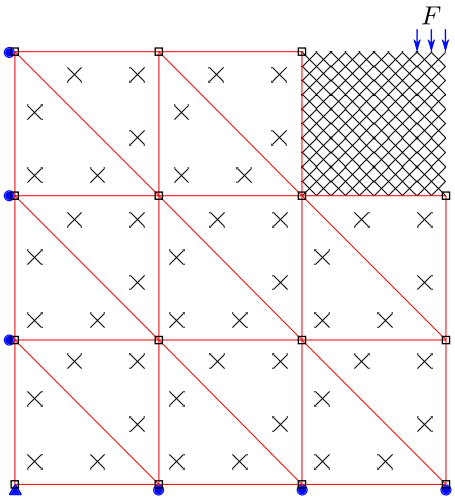

Figure 4: Illustration of summation in the generalized QC method. □ denote the nodes of the IPEs.

3 Adaptive scheme

This section presents the novel adaptive scheme, including the proposed refinement indicator. The adaptive scheme can be used for both conventional as well as generalized QC frameworks.

The adaptive scheme is proposed in this contribution to achieve *refinement*, coarsening being part of future work. Refinement involves both the refinement of IPEs into smaller IPEs and the transformation of IPEs into FRDs. Consequently, it hinges on the following: (1) the discretization of IPEs is automatically adjusted, (2) the size of FRDs is automatically increased, and (3) FRDs are automatically created.

3.1 Refinement indicator

In this section, a new refinement indicator is proposed. The indicator quantifies energy discrepancies at the surfaces of IPEs (IPE edges in 2D) and it is specified for two situations. In the first situation, the *energy discrepancy* is measured for

the interface between two adjacent IPEs. Such an interface is termed as an *IPE-IPE interface*. In the second situation, the *energy discrepancy* is measured for the interface between an IPE and a neighboring FRD. This type of interface is termed as an *IPE-FRD interface*.

At each IPE-IPE interface, a cell is placed at the center of the interface (see Fig. 5a for 2D illustration), referred to as *signaling cell*. This cell does not contribute to the governing equations (i.e. its beams are not sampling beams), it is merely used to decide whether the two IPEs need to be refined or not.

The DoFs of the beams in a signaling cell are first assumed to be completely governed by the first IPE (this involves interpolation as well as extrapolation because part of the signaling cell is inevitably outside the governing IPE (see Fig. 5a)) and its stored energy, E_1, is determined. Second, the DoFs of the beam nodes in the signaling cell are interpolated/extrapolated according to the second IPE. Its stored energy, E_2, is again quantified and the following measurement for energy discrepancy is then computed:

$$\kappa = \frac{|E_1 - E_2|}{\frac{1}{2}(E_1 + E_2)}. \tag{11}$$

In the ideal theoretical case there would be no energy discrepancy.

For each IPE-FRD interface, a signaling cell is also centered at the interface (see Fig. 5b). The DoFs of the signaling cell's beam nodes are now only governed by a single IPE. Accordingly, the energy stored in each beam of the cell is computed. Meanwhile, due to the summation rule (Section 2.2), there are numerous *sampling beams of FRD*, which intersect the IPE-FRD interface and/or touch the IPE-FRD interface (i.e. their beam nodes are located on the interface).

Of each FRD beam intersecting (and touching) the IPE-FRD interface, the beam type is determined according to the beam type classification. Then, the

average stored energy of each beam type is calculated according to Table 1. Let $\bar{E}_{\text{uc}}$ and $\bar{E}_{\text{int}}$ be the average beam energy for a certain type of beam. $\bar{E}_{\text{uc}}$ is obtained by averaging the energies of the corresponding type of beams in the signaling cell. $\bar{E}_{\text{int}}$ is obtained by averaging the energies of the corresponding type of beams among the aforementioned sampling beams of FRD. The energy discrepancy is first evaluated according to Eq. (11) for each type of beam elements that exist among the *intersecting/touching sampling beams of FRDs*. Subsequently, all energy discrepancies (κ^i in Table 1) are averaged. This averaged energy discrepancy is used to indicate whether or not refinement is required.

It is worth noting that, the evaluation of the energy discrepancy for the IPE-IPE/IPE-FRD interfaces follows different logics. For IPE-IPE interfaces, the energies of all beams in the signaling cell are summed from both sides of the interface and then the deviation of the total energy is compared (i.e. the energies are summed and then the error is computed). For IPE-FRD interfaces, the energy errors of individual beam types are first computed and then the errors are averaged. The reason for a different treatment of IPE-FRD interfaces is that, from the IPE side of the IPE-FRD interface, all of the beam types are present because of the signaling cell. From the FRD side of the IPE-FRD interface, it is possible that only a subset of beam types are present among the sampling beams that 'intersect/touch' the interface. Therefore, comparing the individual deviations for existent beam types and then averaging the deviations becomes more reasonable.

In summary, refinement takes place:

- If $\kappa > \kappa_{\text{tol}}$ for a IPE-IPE interface, both IPEs are refined. If the volume of a newly created IPE is below the threshold V_{tol}, the newly created IPE is transformed into an FRD.

- If $\kappa > \kappa_{\text{tol}}$ for a IPE-FRD interface, the relevant IPE is fully resolved.

Beam type	Averaged beam strain energy		Energy discrepancy
	From the signaling cell that is centered on IPE-FRD interface	From the sampling beams with $\omega = 1$ that cross IPE-FRD interface	
1	$\bar{E}^1_{\text{uc}} = \frac{1}{n^1_{\text{uc}}} \sum_{j=1}^{n^1_{\text{uc}}} E^1_j$	$\bar{E}^1_{\text{int}} = \frac{1}{n^1_{\text{int}}} \sum_{j=1}^{n^1_{\text{int}}} E^1_j$	$\kappa^1 = \frac{\lvert \bar{E}^1_{\text{uc}} - \bar{E}^1_{\text{int}} \rvert}{\frac{1}{2}(\bar{E}^1_{\text{uc}} + \bar{E}^1_{\text{int}})}$
2	$\bar{E}^2_{\text{uc}} = \frac{1}{n^2_{\text{uc}}} \sum_{j=1}^{n^2_{\text{uc}}} E^2_j$	$\bar{E}^2_{\text{int}} = \frac{1}{n^2_{\text{int}}} \sum_{j=1}^{n^2_{\text{int}}} E^1_j$	$\kappa^2 = \frac{\lvert \bar{E}^2_{\text{uc}} - \bar{E}^2_{\text{int}} \rvert}{\frac{1}{2}(\bar{E}^2_{\text{uc}} + \bar{E}^2_{\text{int}})}$
...	...	...	...
i	$\bar{E}^i_{\text{uc}} = \frac{1}{n^i_{\text{uc}}} \sum_{j=1}^{n^i_{\text{uc}}} E^i_j$	$\bar{E}^i_{\text{int}} = \frac{1}{n^i_{\text{int}}} \sum_{j=1}^{n^i_{\text{int}}} E^i_j$	$\kappa^i = \frac{\lvert \bar{E}^i_{\text{uc}} - \bar{E}^i_{\text{int}} \rvert}{\frac{1}{2}(\bar{E}^i_{\text{uc}} + \bar{E}^i_{\text{int}})}$
...	...	...	...
Average	–	–	$\kappa = \frac{1}{b} \sum_{i=1}^{b} \kappa^i$

Table 1: Determination of energy discrepancy for a IPE-FRD interface. E^i denotes the strain energy of a type i beam element. n^i_{uc} and n^i_{int} denote the numbers of type i beam elements in the signaling cell and among the intersecting (and touching) FRD sampling beams, respectively. b denotes the number of different beam types.

3.2 Refinement of the spatial discretization

Once the refinement criterion identifies which IPEs need refinement, a refinement algorithm governs *how* the IPEs will be refined or transformed into FRDs. It must be noted that we want to avoid 'hanging' IPE nodes (see Fig. 6). Usually with a conforming discretization the IPE nodes are shared with their other neighboring IPEs, but the central IPE node does not belong to the bottom IPE. We call this IPE node a hanging IPE node. The hanging nodes are avoided because they complicate the refinement algorithm in the presented work.

The refinement algorithm obviously depends on the type of IPE kinematics and the used finite element shape functions. Different IPE orders are employed in QC frameworks: first and higher order triangular finite element shape functions in 2D [5, 6, 11, 30, 34, 41, 46] and linear tetrahedral and hexahedral shape functions in 3D [13, 38, 41]. A *linear tetrahedral interpolation* is used in this work for the 3D IPEs and the refinement algorithm is an extension of the one

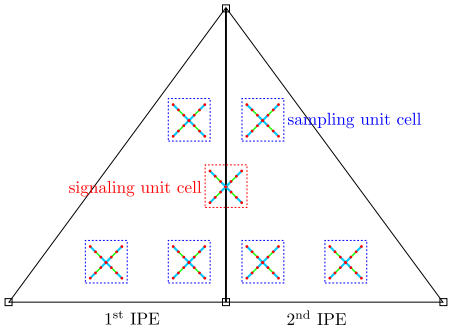

(a) IPE-IPE interface.

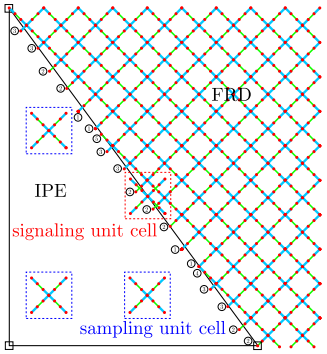

(b) IPE-FRD interface. ⓘ indicates the types of the intersecting sampling beams of FRD.

Figure 5: The scenarios in which the energy discrepancy is measured to drive IPE refinement. □ denote the nodes of the CGDs.

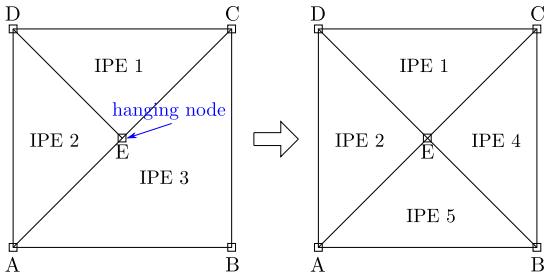

Figure 6: Illustration of hanging IPE node and the solution to avoid it. □ denote the nodes of the IPEs.

proposed by Suárez et al. [43]. The additional originality compared to [43] is that if the volume of a newly created IPE is below V_{tol}, the newly created IPE becomes an FRD. The pseudo code of the refinement algorithm is detailed in

Alg. 1. It is worth noting that a correction step could be added to the refinement algorithm to ensure mesh quality (although it is not done in the presented work) since longest edge bisection is prone to yield poor IPE aspect ratios in general.

Algorithm 1: Refinement algorithm

Input: τ – Tet(tetrahedral) IPEs before refinement
Input: $\tau_{\mathbf{r}}$ – Tet IPE(s) to be refined
Output: τ – Tet IPEs after refinement

```
for each tet t ∈ τ_r do
    Divide t into two tets from the midpoint of the longest edge of t;
    Update τ;
Identify hanging IPE nodes in τ and collect them in set L;
while L ≠ ∅ do
    Let p be a hanging node in set L;
    Let e be the edge on which p is located;
    Let M be the set of tets that share edge e (excluding the tets that have
      resulted in the creation of p);
    for each tet t ∈ M do
        Divide t into two tets from the midpoint of the longest edge of t;
        Update τ;
    Identify hanging nodes in τ and collect them in set L;
for each tet t ∈ τ do
    Let V_t be the volume of t;
    if V_t < V_tol then
        Transform t into FRD;
```

3.3 Adaptive scheme

This section presents the proposed adaptive scheme. Table 2 lists a glossary of symbols that are used in the pseudo code of the adaptive scheme of Alg. 2. Also for better illustration, the concepts of FRDs, CGDs, IPEs, IPE nodes, IPE-IPE interface and IPE-FRD interface are illustrated in Fig. 7.

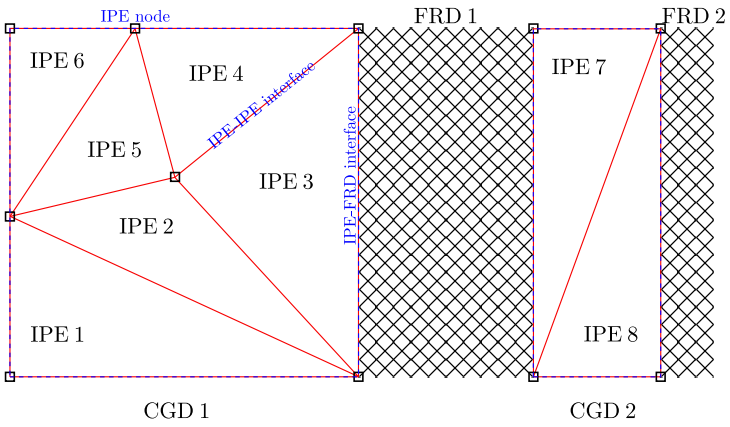

Figure 7: Illustration of key concepts of the adaptive QC method. Inside each IPE, kinematic interpolation using FE shape functions is performed.

Symbol	Description
t_{k}	The k^{th} time step in a Newton scheme.
$\mathbf{\Omega}_{\mathrm{k}}^{\mathrm{FRD}}$	The FRDs at t_{k}.
$\partial\mathbf{\Omega}_{\mathrm{k}}^{\mathrm{FRD}}$	The boundary of the FRDs at t_{k}.
$\mathbf{\Omega}_{\mathrm{k}}^{\mathrm{CGD}}$	The CGDs at t_{k}.
$\partial\mathbf{\Omega}_{\mathrm{k}}^{\mathrm{CGD}}$	The boundary of the CGDs at t_{k}.
τ_{k}	The IPE & FRD configuration at t_{k}.
$\mathbf{S}^{\mathrm{k}}$	The set of sampling beams at t_{k}.
$\mathbf{u}_{\mathrm{r}}^{\mathrm{k}}$	The reduced DoFs after *interpolation* at t_{k}.
$\mathbf{f}_{\mathrm{int}}^{\mathrm{k}}$	The internal force vector corresponding to $\mathbf{u}_{\mathrm{r}}^{\mathrm{k}}$.
$\mathbf{\Phi}_{\mathrm{k}}^{\mathrm{k\text{-}1}}$	The interpolation matrix relating $\mathbf{u}_{\mathrm{r}}^{\mathrm{k}}$ to $\mathbf{u}_{\mathrm{r}}^{\mathrm{k\text{-}1}}$.
κ_{tol}	The threshold of the energy discrepancy.
V_{tol}	The minimally acceptable area/volume of a IPE.

Table 2: Glossary of the notations.

Two issues in Alg. 2 are are clarified here. First, the interpolation matrix $\mathbf{\Phi}_{\mathrm{k}}^{\mathrm{k\text{-}1}}$ denotes the matrix necessary to give an appropriate initial guess to a new (i.e. refined) IPEs & FRD configuration in order to solve the current time step (t_{k}) in a Newton algorithm. This is accomplished by projecting the converged solution at $t_{\mathrm{k\text{-}1}}$, $\mathbf{u}_{\mathrm{r}}^{\mathrm{k\text{-}1}}$, as initial guess for time step t_{k} with the new IPE & FRD configuration, $\mathbf{u}_{\mathrm{r}}^{\mathrm{k}}$. In other words, the only goal of $\mathbf{\Phi}_{\mathrm{k}}^{\mathrm{k\text{-}1}}$ is to equip newly created

Algorithm 2: Adaptive scheme

Initialization: configure $\mathbf{\Omega}_0^{\mathrm{FRD}}$, $\mathbf{\Omega}_0^{\mathrm{CGD}}$, τ_0, S^0, set $\mathbf{u}_{\mathrm{r}}^0 = \mathbf{0}$, $\mathbf{f}_{\mathrm{int}}^0 = \mathbf{0}$.
for *k = 1,2,…,n* **do**
  Inherit configurations of previous time step, i.e. $\mathbf{\Omega}_{\mathrm{k}}^{\mathrm{FRD}} = \mathbf{\Omega}_{\mathrm{k\text{-}1}}^{\mathrm{FRD}}$, $\mathbf{\Omega}_{\mathrm{k}}^{\mathrm{CGD}} = \mathbf{\Omega}_{\mathrm{k\text{-}1}}^{\mathrm{CGD}}$, $\tau_{\mathrm{k}} = \tau_{\mathrm{k\text{-}1}}$, $S^{\mathrm{k}} = S^{\mathrm{k\text{-}1}}$, $\mathbf{u}_{\mathrm{r}}^{\mathrm{k}} = \mathbf{u}_{\mathrm{r}}^{\mathrm{k\text{-}1}}$, $\mathbf{f}_{\mathrm{int}}^{\mathrm{k}} = \mathbf{f}_{\mathrm{int}}^{\mathrm{k\text{-}1}}$.
  Apply boundary conditions of t_{k} to $\partial\mathbf{\Omega}_{\mathrm{k}}^{\mathrm{FRD}}$ and $\partial\mathbf{\Omega}_{\mathrm{k}}^{\mathrm{CGD}}$.
  Equilibrate the unbalanced system by solving Eq. (9).
  Evaluate energy discrepancy κ for IPE-IPE interfaces in τ_{k}, identify the IPEs with $\kappa > \kappa_{\mathrm{tol}}$ and collect them in set τ_{refine}.
  while $\tau_{refine} \neq \emptyset$ **do**
    Apply Alg. 1.
    Update $\mathbf{\Omega}_{\mathrm{k}}^{\mathrm{FRD}}$, $\mathbf{\Omega}_{\mathrm{k}}^{\mathrm{CGD}}$, τ_{k}, S^{k}.
    Compute interpolation matrix $\mathbf{\Phi}_{\mathrm{k}}^{\mathrm{k\text{-}1}}$, reset initial guess as $\mathbf{u}_{\mathrm{r}}^{\mathrm{k}} = \mathbf{\Phi}_{\mathrm{k}}^{\mathrm{k\text{-}1}}\mathbf{u}_{\mathrm{r}}^{\mathrm{k\text{-}1}}$, update $\mathbf{f}_{\mathrm{int}}^{\mathrm{k}}$ according to Eq. (6).
    Equilibrate the unbalanced system by solving Eq. (9).
    Evaluate energy discrepancy κ for IPE-IPE interfaces in τ_{k}, identify the IPEs with $\kappa > \kappa_{\mathrm{tol}}$ and collect them in set τ_{refine}.
  Evaluate energy discrepancy κ for IPE-FRD interfaces in τ_{k}, identify the IPEs with $\kappa > \kappa_{\mathrm{tol}}$ and collect them in set τ_{resolve}.
  while $\tau_{resolve} \neq \emptyset$ **do**
    Transform the IPEs in τ_{resolve} into FRDs.
    Update $\mathbf{\Omega}_{\mathrm{k}}^{\mathrm{FRD}}$, $\mathbf{\Omega}_{\mathrm{k}}^{\mathrm{CGD}}$, τ_{k}, S^{k}.
    Compute interpolation matrix $\mathbf{\Phi}_{\mathrm{k}}^{\mathrm{k\text{-}1}}$, reset initial guess $\mathbf{u}_{\mathrm{r}}^{k} = \mathbf{\Phi}_{\mathrm{k}}^{\mathrm{k\text{-}1}}\mathbf{u}_{\mathrm{r}}^{\mathrm{k\text{-}1}}$, update $\mathbf{f}_{\mathrm{int}}^{\mathrm{k}}$ according to Eq. (6).
    Equilibrate the unbalanced system by solving Eq. (9).
    Evaluate energy discrepancy κ for IPE-FRD interfaces in τ_{k}, identify the IPEs with $\kappa > \kappa_{\mathrm{tol}}$ and collect them in set τ_{resolve}.
  Store output data of current time step: $\mathbf{\Omega}_{\mathrm{k}}^{\mathrm{FRD}}$, $\mathbf{\Omega}_{\mathrm{k}}^{\mathrm{CGD}}$, τ_{k}, S^{k}, $\mathbf{u}_{\mathrm{r}}^{\mathrm{k}}$, $\mathbf{f}_{\mathrm{int}}^{\mathrm{k}}$.

nodes (i.e. new beam nodes in FRDs and new IPE nodes) with an initial guess that is in accordance with the converged solution at $t_{\mathrm{k\text{-}1}}$ for the previous IPE & FRD configuration.

A second issue that needs clarification is that the energy discrepancy is first measured for IPE-IPE interfaces (lines 6–12 in Alg. 2) and subsequently for IPE-FRD interfaces (lines 13–19). The reason to split the measuring of the energy discrepancy in two stages is that IPE refinement only results in a few more DoFs and sampling beams, whereas transforming IPEs into FRDs yields considerably more DoFs and sampling beams. It is therefore computationally more beneficial to prioritize the refinement of the IPEs.

3.4 Choice of the adaptivity parameters

The appropriate values for the threshold of the energy discrepancy, κ_{tol}, and the volume threshold to fully resolve an IPE, V_{tol}, are case specific.

Different shapes of cells, beam discretization of cells and sizes of lattices were observed to require different [κ_{tol}, V_{tol}] sets. The choice of κ_{tol} and V_{tol} actually depends on the trade-off between the accuracy of the results and the computational saving. In this section some recommendations for tuning the adaptivity parameters are given.

Generally, a small κ_{tol} promotes the accuracy of the simulation because the energy discrepancy across the IPE-IPE and IPE-FRD interfaces is reduced. However, excessively small κ_{tol} risks over refinement for the adaptive GQC (i.e. tendency for large FRD and small IPEs) and thus compromises the computational saving.

In a similar fashion V_{tol} should not be too large, because this would result in the direct transformation of large IPEs into FRD (promoting a DNS like simulation). On the other hand, V_{tol} should not be too small, because a too low value can result in IPEs having more sampling beams than the underlying number of lattice beams in the IPE volume, i.e. the computational effort would be larger for the IPE than considering the same volume as FRD. To avoid this,

one possible solution could be to track the actual number of lattice beams inside an IPE on the fly to decide whether or not fully resolving it. This can however be a computationally expensive practice and may be considered in future work. A second, simpler option used in this work, is to set the lower bound of V_{tol} as the product between the volume of one cell and the number of Gauss quadrature points in an IPE. A higher V_{tol} than this lower bound is used in the simulations. It is noteworthy that, as will be shown in Table 3 of Section 4.2, for a given κ_{tol} in the simulations, choosing a V_{tol} close to its lower bound was observed to yield more accurate results when compared to DNS. This can be explained by a small V_{tol} resulting in small IPEs around the FRDs creating a kinematically rich (but computationally efficient) zone near the region of main interest, as well as a sound transition from FRDs to large IPEs through IPEs with gradually increasing size further from this region. A possible as a worst case scenario, too small V_{tol} may result in so small IPEs, that the signaling cells on the edges extend into the neighboring IPEs. Yet no such singular case was observed under the chosen V_{tol} in the presented work.

The optimal values of κ_{tol} and V_{tol} were chosen in this work by trial-running a few increments in the AGQC simulation using several options of κ_{tol} and V_{tol} and observing the resulting range and extent of the refinement. The improvement of the computational saving and the difference in accuracy can then be accessed by comparing the overall response of different AGQC simulations (as explained in Section 4.2) to choose the most promising [κ_{tol}, V_{tol}] set.

4 Application of adaptive GQC

In this section, five numerical examples are presented. The example of Section 4.1 demonstrates that the proposed refinement indicator is insensitive to uniform deformation and rigid body rotation. The example of Section 4.2 illustrates the

capabilities of the adaptive generalized QC method by indenting a BCC lattice, and a procedure for choosing $[\kappa_{\text{tol}}, V_{\text{tol}}]$ is proposed. The examples of Section 4.3 and 4.4 show that the adaptive scheme is also able to treat on the fly progressive refinement during the simulation of a BBC and a Kelvin lattice scratched by a rigid sphere. The example of Section 4.5 showcases the ability of adaptive GQC to simulate the scratch of a large Kelvin lattice, which is computationally too demanding for DNS.

The beam representation of the BCC cell we adopt is shown in Fig. 8. All beams have circular cross sections. However, the diameter of the red beams is 0.230 mm, whereas that of the blue beams is 0.185 mm. The beams are formulated as linear elastic, geometrically non-linear co-rotational beams, with a Young's modulus of 140 GPa and a Poisson's ratio of 0.3. These geometrical and material parameters are the same as used in [42].

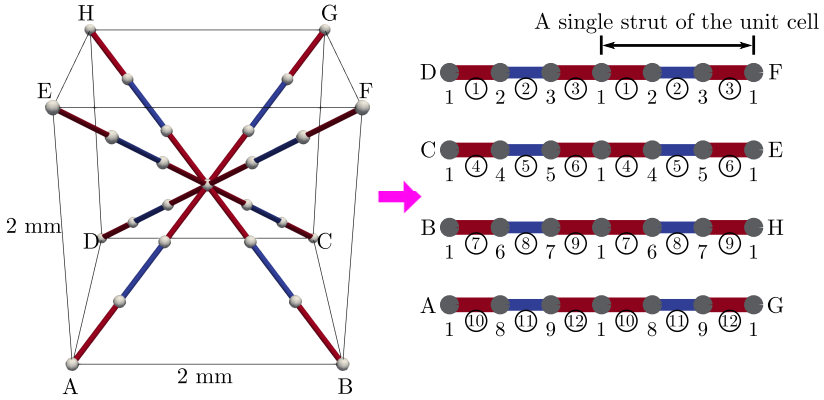

Figure 8: Beam representation of a BCC cell. All blue beams are given the same geometrical and material parameters and the red beams are given their own geometrical and material parameters. Beam node (•) types are indicated as $1-9$. Beam types are indicated as ①$-$⑫.

The beam representation of the Kelvin cell we consider is shown in Fig. 9. Each of the 36 struts, which are of equal length, is represented using one beam finite element. Each beam is assumed to have a circular cross section with a

diameter of 0.230 mm, a Young's modulus of 140 GPa and a Poisson's ratio of 0.3.

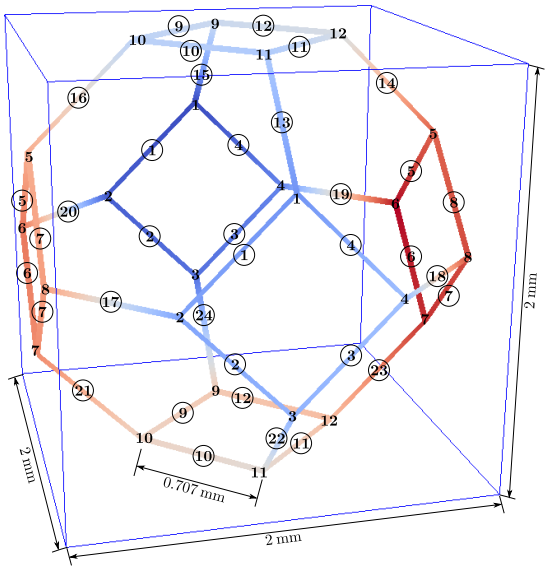

Figure 9: Beam representation of the Kelvin cell. Beam node types are indicated as 1 – 12. Beam element types are indicated as ① – ㉔.

In order to apply *the interpolation* of the generalized QC method, the beam nodes of a cell are classified into different types. Differentiated by the beam node types of both ends, the beam elements in a cell are also categorized into several types. The classification of beam nodes and beam elements are indicated in Fig. 8 for the BCC cell and Fig. 9 for the Kelvin cell.

It is also worth noting that the lattice is obtained by repeating the cell in X, Y, Z directions. For BCC cell, the stacking will not lead to overlapping struts. But for the Kelvin cell, there will be overlapping struts (i.e. the beams of types ① – ⑫). When we use this cell as the sampling cell at the Gauss quadrature points in IPEs, the overlapping beams are assigned half of the energy. When a Kelvin cell is used as the signaling cell, these overlapping beams are considered with their actual diameter for the measurement of the elastic strain energy.

Linear tetrahedral IPEs are used in all simulations. Five GQPs per IPE are used to generate sampling beams, because this was observed to be the minimum number that guarantees convergence [13].

4.1 Uniaxial compression of a BCC lattice

This section aims to show that the new refinement indicator does not trigger refinement if homogeneous deformation (up to the occurrence of buckling in the case of compression) and/or rigid body rotation occur. As will be shown, the refinement in case of homogeneous deformation is not needed since the GQC can accurately capture the force–displacement curve. However, for refinement indicators that are based on measuring the deformation gradient tensor (e.g. [38]), refinement will nevertheless be triggered for homogeneous deformation, although it is unwanted.

Particularly, we study uniform compression. The studied BCC lattice is illustrated in Fig. 10, together with the FRD and IPEs. Two IPE-FRD interfaces and four IPE-IPE interfaces can be distinguished for the model of Fig. 10a, 10b. Two IPE-FRD interfaces and six IPE-IPE interfaces are present in the model of Fig. 10c, 10d. During the simulation the energy discrepancies at all these interfaces are monitored.

The DNS (i.e. full FRD representation of the model) and the adaptive generalized QC method results are compared. Fig. 11 shows that both force-displacement curves practically match.

Fig. 11 presents the evolutions of the energy discrepancies at the different interfaces. The energy discrepancies at the IPE-IPE interfaces remain zero throughout the loading process. The energy discrepancies of the IPE-FRD interfaces are non-zero, yet they are relatively small. The reason is a (small) error induced by the summation rule, i.e. the ways of constructing the governing

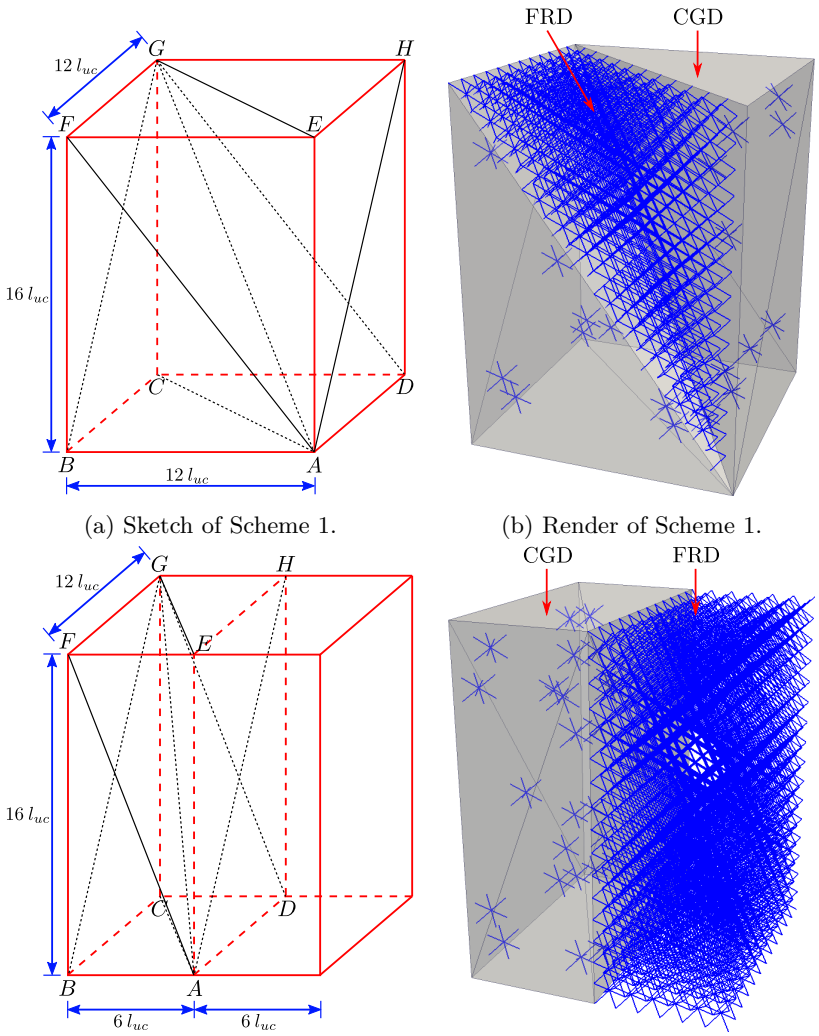

(a) Sketch of Scheme 1.

(b) Render of Scheme 1.

(c) Sketch of Scheme 2.

(d) Render of Scheme 2.

Figure 10: The interpolation schemes for the lattice under uniaxial compression. l_{uc} denotes the length of one cell, which equals 2 mm.

equations in the CGDs and the FRDs are different.

It is emphasized that because this error is inherent to the method, the energy discrepancy remains practically the same during loading. Hence, no refinement is triggered in case of homogeneous deformation (assuming κ_{tol} is set high enough).

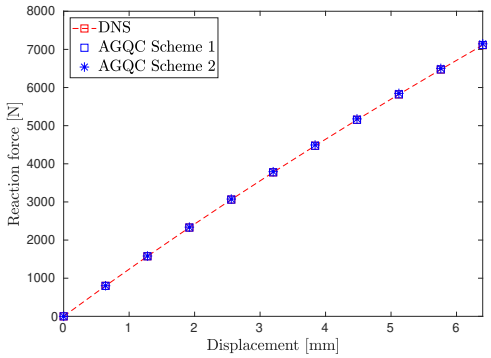

Figure 11: Force-displacement response of the lattice under uniaxial compression.

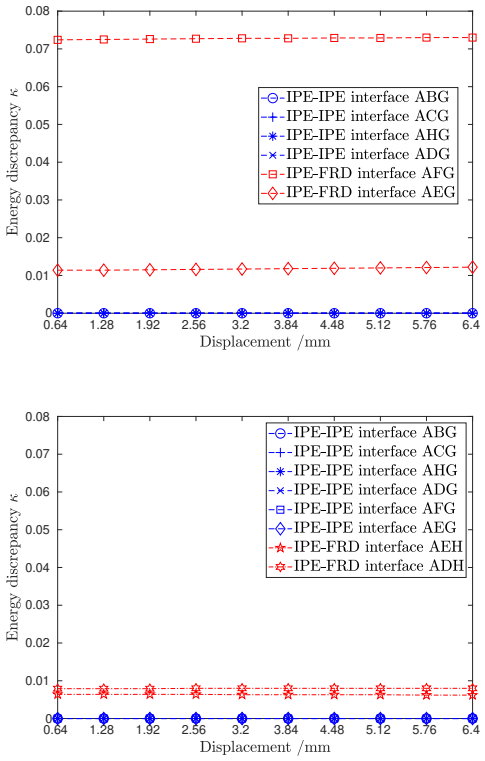

Figure 12: Energy discrepancies for different interfaces. Top: scheme 1 (Fig. 10a, 10b), bottom: scheme 2 (Fig. 10c, 10d).

It is also worth noting that the refinement indicator is insensitive to rigid body translations and rotations because of using 3D co-rotational beam finite elements to represent the lattice structure, capable of handling large displacements and finite rotations [3, 4].

Regrettably the simulation could not continue until beam buckle because of a lack of convergence at large compression strain. In the scenario of compressing a lattice uniformly in a regime prior to buckling, the affine interpolation introduced in the CGDs suffices to map the distribution of kinematic variables. Refinement is thus not needed for this pre-buckling stage of loading. However, when buckling comes into play in the CGDs, the relevant CGDs should be fully resolved to enable sufficient kinematic richness to capture the buckling.

In case of the refinement indicator proposed here, the value of the refinement indicator remains constant and small throughout the uniform compression procedure until a divergence of simulation occurs at large compression strain. The divergence implies the occurrence of buckling in the coarse-grained domain and the necessity to change from coarse-grained domains to fully-resolved domains. It is believed that monitoring the buckling states of the sampling cells (or checking the loss of structural stiffness for the interpolation element) in the CGDs would be a future supplement and remedy to the proposed refinement indicator.

However the constant and small properties of the proposed refinement indicator in the case of uniform deformation can still be considered as an advantage to some extent. It is true that this advantage is shadowed during the uniform compression test, for which an supplementary check of cell buckling state should be introduced. In scenarios such as uniform stretch however, the refinement indicator leads to no undesired refinement.

For the following numeric examples, the induced strains are local and do not cause sampling beams of CGDs to buckle.

4.2 Spherical indentation of a BCC lattice

In this section, the adaptive generalized QC method is applied to simulate the indentation of a BCC lattice with a rigid sphere. The model consists of $36 \times 36 \times 36$ BCC cells (see Fig. 13). The radius of the rigid sphere (r_{sp}) is 10 mm, which is 5 times the length of one cell (l_{uc}). As indentation occurs in the center of the model, both the lattice itself and the boundary conditions are symmetric, only a quarter of the model was considered thanks to symmetrical boundary conditions. As is indicated in Fig. 13, the beam nodes on the bottom are constrained from moving in the normal direction (i.e. $U_z = 0$). For the two symmetrical faces (i.e. the yellow and green faces in Fig. 13), beam nodes are constrained from normal displacement and out-of-plane rotations (i.e. $U_y = \theta_x = \theta_z = 0$ for the green face, $U_x = \theta_y = \theta_z = 0$ for the yellow face). All the other DoFs of the beam nodes are free. The final indentation depth is set to 2 mm, which equals the cell length. The indentation is achieved in 100 increments.

Contact between the lattice and the rigid sphere is modeled using a node-to-segment scheme. The penalty approach is used to incorporate the unilateral frictionless contact conditions [16, 17, 25, 28, 49]. The penalty parameter is set to 10^3 N/mm in all simulations in this contribution and not updated during the simulation. Note that the contact between beams is not considered for any of the simulations in this contribution. This is because when the beam to beam contact starts to govern the response, the lattice has been substantially deformed, while simulations here are expected to remain in the elastic domain.

Two non-adaptive QC simulations are considered in order to obtain more reference results than only those of the DNS. In the first non-adaptive QC simulation, an FRD of $6 \times 6 \times 6$ cells is incorporated below the rigid sphere (Fig. 14a). In the second non-adaptive QC simulation, the FRD is enlarged to $12 \times 12 \times 12$ cells (Fig. 14b).

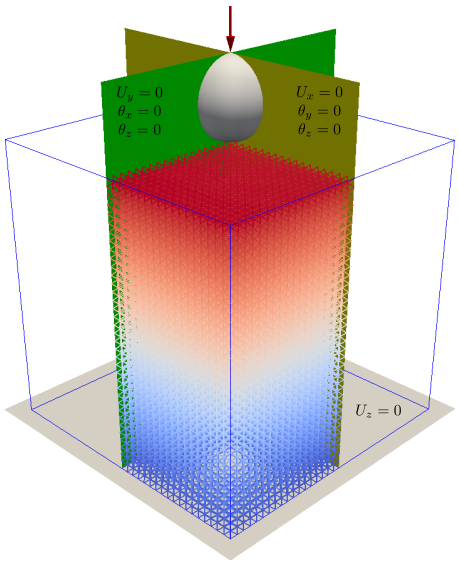

Figure 13: Quarter model for the indentation of a BCC lattice.

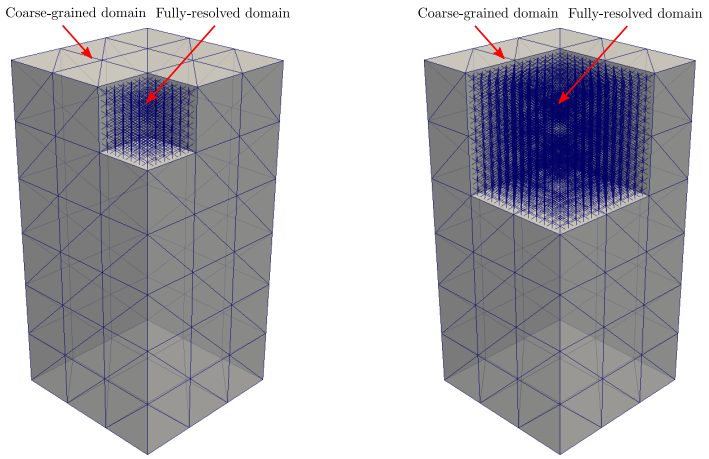

(a) FRD $6\,l_{uc} \times 6\,l_{uc} \times 6\,l_{uc}$ (b) FRD $12\,l_{uc} \times 12\,l_{uc} \times 12\,l_{uc}$

Figure 14: Interpolation schemes of the lattice under indentation. l_{uc} denotes the length of one cell.

For the adaptive generalized QC simulations, the scheme of Fig. 14a is chosen as the initial configuration. The control parameters of the adaptivity are set as follows. To study the influence of κ_{tol}, we fix V_{tol} to be five times the volume

of a cell (i.e. $5\,l_{uc}^3$) and set κ_{tol} to be 0.8, 0.6, 0.4, 0.2 in different simulations. To study the influence of V_{tol}, we fix κ_{tol} to be 0.2, 0.4 and set V_{tol} to be $5\,l_{uc}^3$, $10\,l_{uc}^3$, $15\,l_{uc}^3$ in successive simulations.

Fig. 15 plots the curves of the normal contact force versus the indentation depth under constant V_{tol} (Fig. 15a) and κ_{tol} (Fig. 15b and 15c) respectively. As can be seen, the force – displacement curves include several kinks that are attributed to the progressive establishment of contacts during the indentation. In other words, the deeper we indent the rigid sphere, the more beam nodes come in contact with the rigid sphere. In Fig. 15a, there are two apparent kinks: kink 1 happens because the number of contact points between the rigid sphere and the lattice jumps from 1 to 3; kink 2 happens because the number of contact points jumps from 4 to 6.

To illustrate the difference between the models, the initial contact stiffness was calculated up to 0.02 mm indentation depth (Fig. 16). The initial stiffness is notably different and it can be used to decide on κ_{tol} in a first few increments: $\kappa_{\text{tol}} = 0.4$ and $\kappa_{\text{tol}} = 0.2$ yield close results (hence $\kappa_{\text{tol}} = 0.4$ could be chosen for a complete simulation).

The value of κ_{tol} has a more significant impact on the accuracy in the considered range compared to V_{tol}. The smaller the values of κ_{tol} and V_{tol} are (within the bounds defined in Section 3.4), the more accurate the result is.

To visualize the refinement procedure throughout the AGQC simulations, Fig. 17 and Fig. 18 monitor three quantities denoted as KV%, SB% and V_{CGD}%. KV% denotes the ratio between the number of DoFs (kinematic variables) in the QC model and the number of DoFs in the DNS. SB% denotes the ratio between the number of sampling beams in the QC model and the number of beams in the DNS. V_{CGD}% denotes the volumetric fraction of CGD.

Table 3 provides a detailed comparison among the different modeling schemes

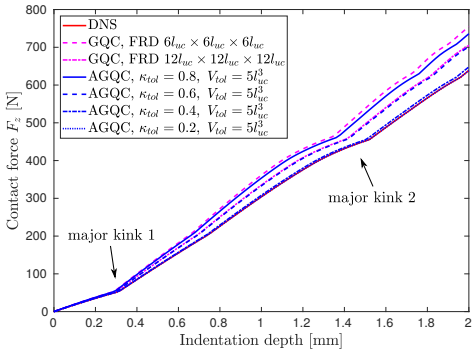

(a) $V_{\text{tol}} = 5\, l_{uc}^3$

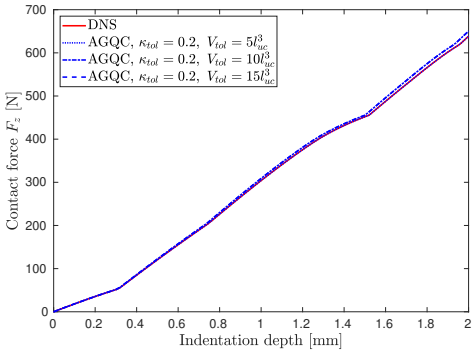

(b) $\kappa_{\text{tol}} = 0.2$

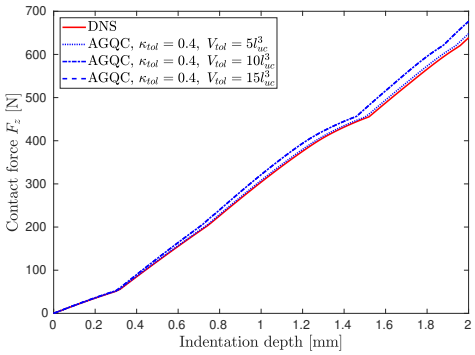

(c) $\kappa_{\text{tol}} = 0.4$

Figure 15: The normal contact force versus the indentation depth. l_{uc} denotes the length of one cell.

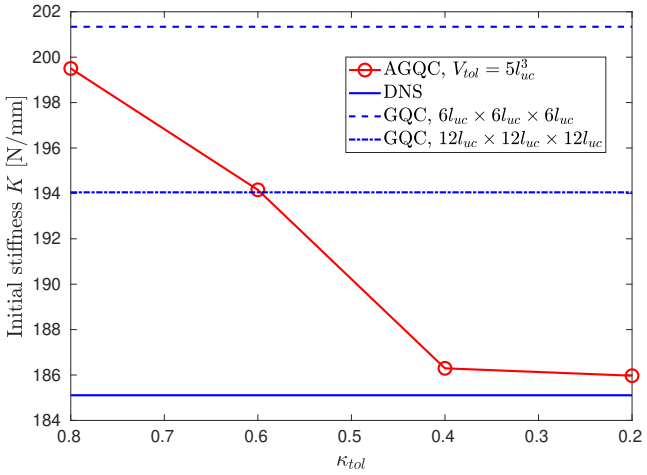

Figure 16: Comparison of initial stiffness of the variant model schemes.

in terms of the model scales, the error and the required computational time. The required computational time is the walltime of running the in-house MATLAB codes on the HPC Hydra (`https://hpc.ulb.be/`). The codes of both AGQC and DNS are parallelized and are running using 12 cores. In Table 3, the DNS result serves as the reference solution. The discrepancy between the results of the different QC models and the DNS solution is quantified as the difference of external work, which is computed from the force-displacement curves in Fig. 15 using the trapezoidal rule. Also, because progressive refinement can be observed in Fig. 17 and Fig. 18, the average number of DoFs, the average number of sampling beams and the average volume fraction of CGDs are shown in Table 3. They are obtained by computing the mean value of the corresponding items out of the 100 increments. We choose to calculate the average values because the number of DoFs, the number of sampling beams and the volume fraction of CGDs can vary from increment to increment during the progressive refinement. Note that in Table 3, not only the absolute values of the DNS are provided, but also the percentage difference between the QC schemes and the

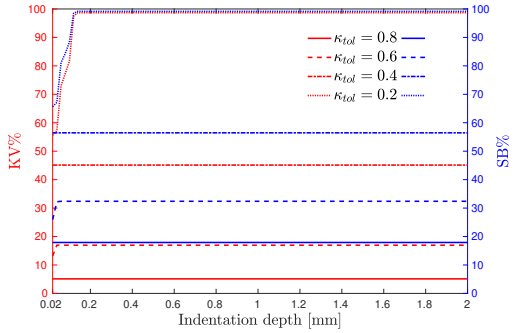

(a) $V_{\text{tol}} = 5\, l_{uc}^3$.

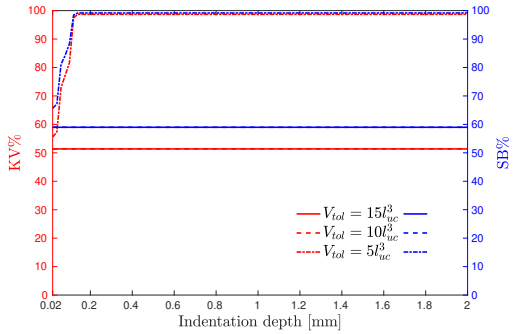

(b) $\kappa_{\text{tol}} = 0.2$. The results of $V_{\text{tol}} = 10\, l_{uc}^3$ and $15\, l_{uc}^3$ are coincident.

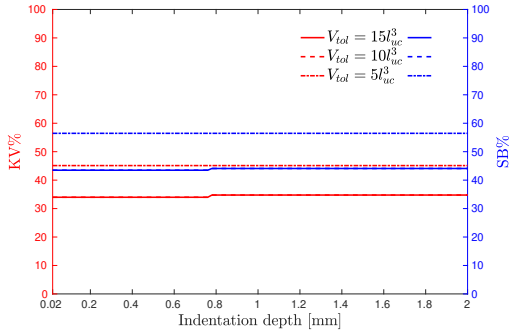

(c) $\kappa_{\text{tol}} = 0.4$. The results of $V_{\text{tol}} = 10 l_{uc}^3$ and $15 l_{uc}^3$ are coincident.

Figure 17: The evolution of KV% and SB% during the AGQC simulations of the indentation of the BCC lattice. l_{uc} denotes the length of one cell. The x axis starts from 0.02 mm because it is the first nonzero increment in the Newton incremental-iterative process.

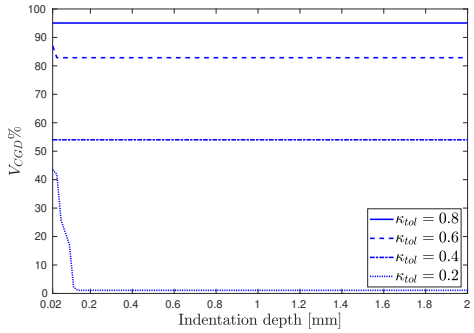

(a) $V_{\text{tol}} = 5\, l_{uc}^3$

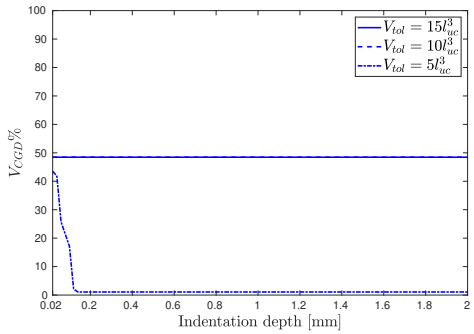

(b) $\kappa_{\text{tol}} = 0.2$. The results of $V_{\text{tol}} = 10l_{uc}^3$ and $15l_{uc}^3$ are coincident.

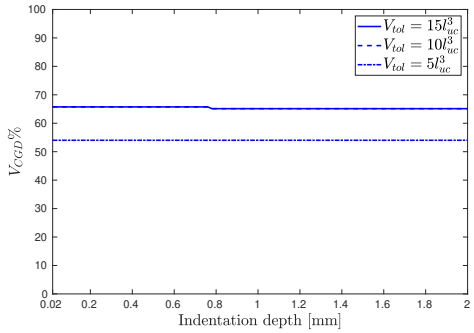

(c) $\kappa_{\text{tol}} = 0.4$. The results of $V_{\text{tol}} = 10l_{uc}^3$ and $15l_{uc}^3$ are coincident.

Figure 18: The evolution of $V_{\text{FRD}}\%$ during the AGQC simulations of the indentation of the BCC lattice. l_{uc} denotes the length of one cell. The x axis starts from 0.02 mm because it is the first nonzero increment in the Newton incremental-iterative process.

DNS are listed. The refined configurations of the IPEs and FRDs at the end of the loading are shown in Fig. 19. Fig. 20 plots the contour of displacement components for the DNS lattice at the end of the loading. Note that negative external work error is observed in Table 3 for the AGQC scheme with $\kappa_{\text{tol}} = 0.2$, $V_{\text{tol}} = 5l_{uc}^3$, which implies more compliant response for the QC simulation. This may be perceived as counter-intuitive as model reduction (of which QC is a type of) reduces the solution space and is expected to stiffen the structural response. This phenomenon is believed to arise from the misalignment between the FRD-CGD interfaces and the cell orientation. This may also interact with the re-distribution arising from the (geometrical) nonlinearity associated with beam formulation. A detailed investigation of the underlying mehcanisms taking place on the FRD-CGD interfaces will be part of future work. Albeit the more compliant response predicted by QC, the deviation is relatively small and one can still considere the GQC modeling as sufficiently accurate.

The following conclusions can be derived from the above results. When a fixed value is chosen for V_{tol}, reducing the value of κ_{tol} can improve the accuracy. When a fixed value is chosen for κ_{tol}, reducing the value of V_{tol} also benefits the accuracy in the studied range of V_{tol}. However, this does not mean that a pair of as small as possible values for κ_{tol} and V_{tol} gives the optimal results. As can be seen from Table 3, when κ_{tol} and V_{tol} are set to 0.2 and $5\, l_{uc}^3$ respectively, excessive refinement is obtained. As a result, almost the whole lattice is fully resolved and because of the refinement procedure (Alg. 2), more computational time is required than that of DNS. The values for κ_{tol} and V_{tol} should be chosen after analyzing their effects on the accuracy and on the computational savings.

For the current example, V_{tol} was fixed first to the lower bound (i.e. $V_{\text{tol}} = 5\, l_{uc}^3$) and one increment was run using different values for κ_{tol}. Observing the initial stiffness (see Fig. 16) allowed choosing $\kappa_{\text{tol}} \leq 0.4$. Then for a fixed

Modeling scheme	External work (N · mm)	Average number of DoFs	Average number of (sampling) beams	Average volume fraction of CGDs (%)	Computational time (hour)
DNS	595.66	1,269,870	279,936	0	8.4
GQC (FRD $6 \times 6 \times 6$)	+17.31%	-97.69%	-84.52%	98.15	-86.90%
GQC (FRD $12 \times 12 \times 12$)	+9.47%	-84.86%	-73.35%	85.19	-76.19%
AGQC $\kappa_{\text{tol}} = 0.8$ $V_{\text{tol}} = 5\, l_{uc}^3$	+14.81%	-94.91%	-82.11%	95.09	-83.33%
AGQC $\kappa_{\text{tol}} = 0.6$ $V_{\text{tol}} = 5\, l_{uc}^3$	+8.84%	-83.23%	-67.84%	83.06	-53.57%
AGQC $\kappa_{\text{tol}} = 0.4$ $V_{\text{tol}} = 5\, l_{uc}^3$	+1.18%	-55.31%	-43.95%	54.44	-41.67%
AGQC $\kappa_{\text{tol}} = 0.4$ $V_{\text{tol}} = 10\, l_{uc}^3$	+5.13%	-65.86%	-56.42%	65.68	-58.33%
AGQC $\kappa_{\text{tol}} = 0.4$ $V_{\text{tol}} = 15\, l_{uc}^3$	+5.13%	-65.86%	-56.42%	65.68	-57.14%
AGQC $\kappa_{\text{tol}} = 0.2$ $V_{\text{tol}} = 5\, l_{uc}^3$	-0.02%	-3.57%	-2.74%	3.48	+33.33%
AGQC $\kappa_{\text{tol}} = 0.2$ $V_{\text{tol}} = 10\, l_{uc}^3$	+1.45%	-49.10%	-41.45%	48.95	-41.67%
AGQC $\kappa_{\text{tol}} = 0.2$ $V_{\text{tol}} = 15\, l_{uc}^3$	+1.45%	-49.10%	-41.45%	48.95	-39.29%

Table 3: Comparison of model scale, accuracy and required computational time among the different modeling schemes. Only the percentage differences compared to the DNS are given for the QC simulations.

κ_{tol}, V_{tol} was increased to $10\, l_{uc}^3$ and $15\, l_{uc}^3$ and the first increment recomputed. Based on the obtained initial stiffness and the intensity of the refinement (e.g. the reduction of the number of DoFs and the number of sampling beams) the refinement parameter set $[\kappa_{\text{tol}},\, V_{\text{tol}}]$ can be chosen. In the current example,

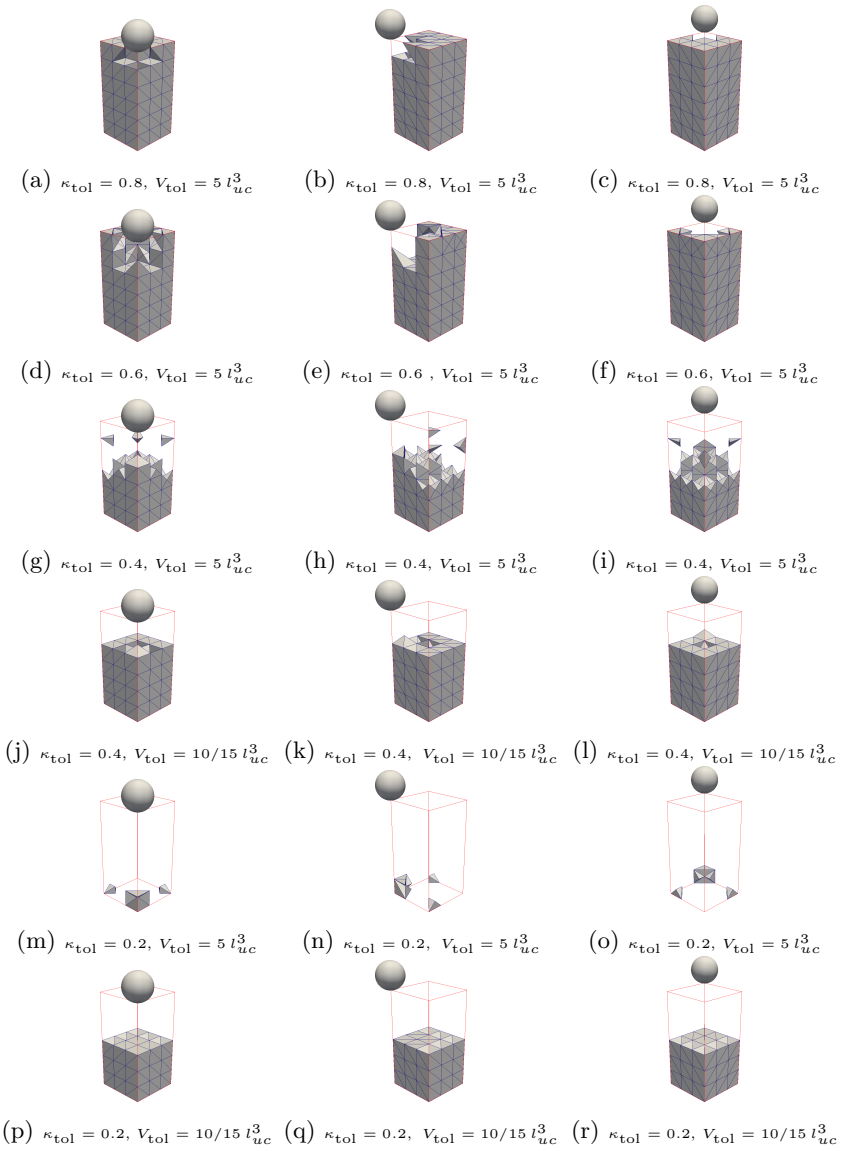

Figure 19: Refined IPEs & FRDs for the indentation example at the last increment. Only the the tetrahedral IPEs in the CGDs are visible, together with red lines outlining the model domain. The void in the model domain represents the FRDs. The left column lists the front views, the middle column lists the side views, the right column lists the back views.

$[\kappa_{\text{tol}} = 0.4,\ V_{\text{tol}} = 10/15\ l_{uc}^3]$ and $[\kappa_{\text{tol}} = 0.2,\ V_{\text{tol}} = 10/15\ l_{uc}^3]$ both achieve a satisfactory balance between the accuracy and the magnitude of model reduc-

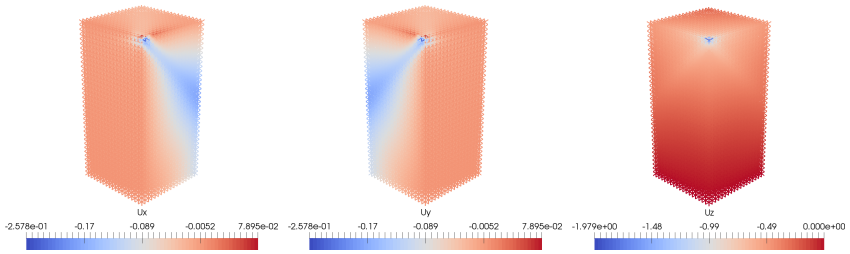

(a) U_x (b) U_y (c) U_z

Figure 20: Contour of displacement components [mm] for the BCC lattice from DNS. The maximum of U_z is not exactly 2 mm because of the penalty treatment of the contact condition.

tion. In Fig. 17, KV% and SB% are below 1 which should be the upper bound of KV% and SB% since it indicates the reduction of model scale after applying QC (this shows that V_{tol} lower bound was chosen appropriately).

When κ_{tol} is 0.2, tweaking the value of V_{tol} from $5\,l_{uc}^3$ to $10\,l_{uc}^3$ presents a significant improvement for the required computational time while the result is still quite accurate. On the contrary, when κ_{tol} is 0.4, tweaking the value of V_{tol} from $5\,l_{uc}^3$ to $10\,l_{uc}^3$ presents a mild improvement for the required computational time but a mild deterioration to the accuracy. In this case, the loss may not outweigh the gain. Also, when κ_{tol} is 0.2/0.4, setting V_{tol} to be $10\,l_{uc}^3$ and $15\,l_{uc}^3$ gave identical results. The above shows the complex interplay between the refinement parameters.

As for this example, no significant progressive refinement was observed. The majority of the refinement is accomplished in the first few increments (see Fig. 17 and 18). This was beneficial because running a few increments for a given pair of κ_{tol} and V_{tol} could be used as a trustworthy indicator for their optimal choice. In simulations where progressive refinement is significant (Section 4.4 & 4.5), trial-running the first few increments was still observed to be able to indicate optimal adaptivity parameters. The rapid and extensive refinement can be explained by BCC lattices that exhibit strongly non-local deformation modes (see Fig. 20,

where the indentation prompts far-reaching strain fluctuation). This can be attributed to the orientations of struts in the BCC cell as the diagonal struts propagate the load along preferential direction.

Note that although the contours of U_x (Fig. 20a) and U_y (Fig. 20b) are more heterogeneous than the contour of U_z (Fig. 20c), the magnitudes of U_x and U_y are much smaller. Therefore, it is the distribution of U_z that can be looked upon as relevant for the refinement of QC modeling. In Fig. 20c, the induced fluctuation of U_z is concentrated in the upper part of the lattice with the lower part of the lattice less significantly impacted. This is the reason why the QC models with $[\kappa_{\text{tol}} = 0.4, V_{\text{tol}} = 5\ l_{uc}^3]$ (Figs 19g, 19h, 19i), $[\kappa_{\text{tol}} = 0.4, V_{\text{tol}} = 10/15\ l_{uc}^3]$ (Figs 19j, 19k, 19l) and $[\kappa_{\text{tol}} = 0.2, V_{\text{tol}} = 10/15\ l_{uc}^3]$ (Figs 19p, 19q, 19r) give relatively accurate results (with the percentage error of external work below 5.13%) by only resolving the upper part of the lattice.

4.3 Scratching a BCC lattice with a rigid sphere

In this section, the adaptive generalized QC method is applied to simulate the scratching of an elastic BCC lattice using a rigid sphere. Fig. 21 presents some geometrical aspects of the simulation. The model consists of $5 \times 150 \times 20$ BCC cells. The radius of the rigid sphere is set be 100 mm, which is 50 times the length of a cell.

The rigid sphere is placed so that its lowest point is 0.02 mm ($0.01\, l_{uc}$) below the top face of the lattice. Symmetry boundary conditions are introduced in order to only consider half of the lattice (Fig. 21). The penalty approach is used to incorporate the frictionless contact conditions between the lattice and the sphere. The boundary conditions are also indicated in Fig. 21b.

It is worth mentioning that the frictionless contact between the beams and sphere, together with the elastic beam constitutive model is oversimplified in

comparison to the real life lattice testing where in addition to contact, beam damage and plasticity play an important role. However, the presented examples intend to assess the adaptive generalized QC's ability to replicate the DNS with lower computational cost - in particular its adaptive part including the capabilities of the refinement indicator. Incorporating a nonlinear material behavior for more physically related results was not the primary concern.

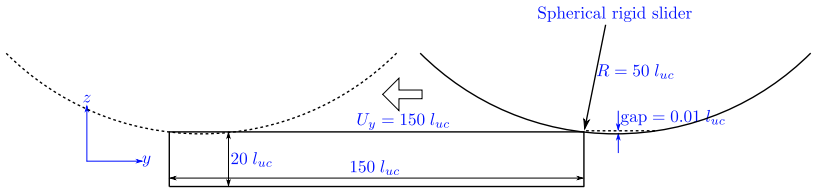

(a) Geometry of the scratch simulation, 2D view. The rigid sphere is moved along the sample surface by $U_y = 150\, l_{uc}$

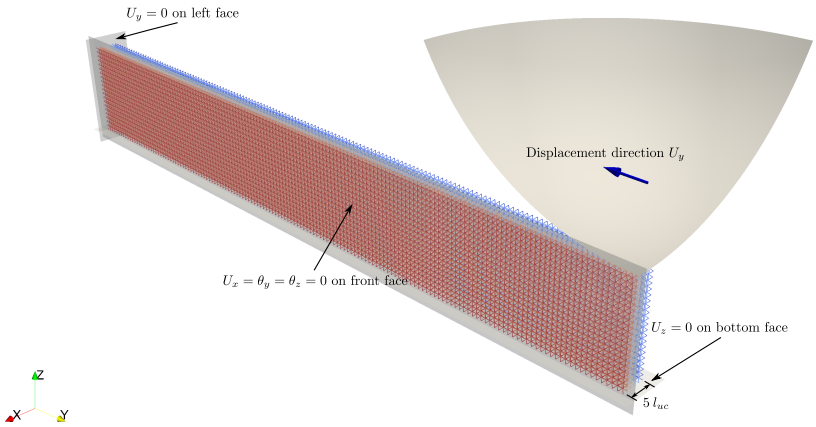

(b) 3D view.

Figure 21: Problem setup for the elastic BCC lattice scratching with a rigid sphere.

In the adaptive QC simulation, V_{tol} is set to five times the volume of a cell and κ_{tol} is set to 0.7 (V_{tol} and κ_{tol} are chosen after studying their marginal improvement like the one in Section 4.2). Fig. 22 depicts the initial configuration of the adaptive generalized QC simulation, where an FRD of $5\, l_{uc} \times 5\, l_{uc} \times 5\, l_{uc}$ is initially used close to the rigid sphere to allow smooth contact establishment.

In all the simulations, 100 increments are adopted.

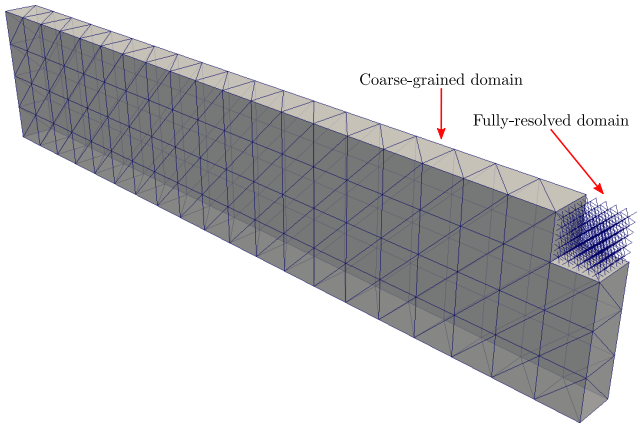

Figure 22: Initial discretization for the QC simulation.

Fig. 23 shows the curves of the vertical contact force versus the horizontal displacement of the rigid sphere. Oscillations can be observed because the lattice is inherently discrete. They correspond to the establishment and loss of contact beam-by-beam in the FRD. Also, the force – displacement curve can be divided into three stages, i.e. the stage of contact establishment ($U_y \leq 50$ mm), the stage of "stable" contact regime ($50\,\text{mm} \leq U_y \leq 250\,\text{mm}$) and the stage of final loss of contact ($U_y \geq 250$ mm). Contact establishment and final loss of contact span a displacement range of 50 mm corresponding to the radius of the rigid sphere. The consistency between the DNS result and AGQC results is better for the stage of final loss of contact compared to the stage of contact establishment because almost the whole AGQC model is fully resolved at this stage.

Fig. 24 illustrates how KV%, SB% and V_{FRD}% (the volumetric fraction of the fully-resolved domains) evolve as the simulation progresses. As can be seen from Fig. 24, during the stage of contact establishment, the portion of the model that is fully resolved leaps to around 90%. This shows that the establishment of contact has far-reaching influence compared to the physical size of the model.

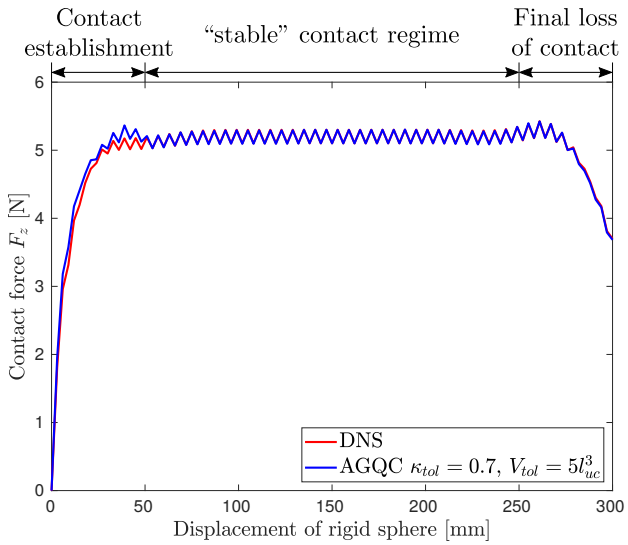

Figure 23: The contact force versus the displacement of the rigid sphere for DNS and AGQC approaches of the BCC lattice.

BCC cells indeed exhibit nonlocal response because of the layout of diagonal struts that provide far-reaching normal force transmission along the diagonal directions. The displacement contours (Figs. 25c, 25f, 25i) illustrate the nonlocal deformation response of the BCC lattice.

Fig. 25 reveals more details of the refinement. As can be seen, the proposed adaptive generalized QC method can successfully adapt the spatial representation of FRDs & IPEs progressively during the simulation. Note that in Figs. 25a and 25d, the left end of the lattice is coarse-grained at $U_y = 3$ mm, while a local FRD emerged at $U_y = 27$ mm. This FRD is clearly isolated from the rest of the FRDs. It shows that the proposed adaptive scheme allows new FRDs to be created where needed besides automatically increasing the sizes of FRDs.

Because of the nonlocal deformation response of of the BCC lattice and the relatively small size of the lattice (so that DNS can be affordable), a large portion of the lattice is fully resolved and the computational saving is not particularly impressive. Naturally, with larger model sizes, more significant computational

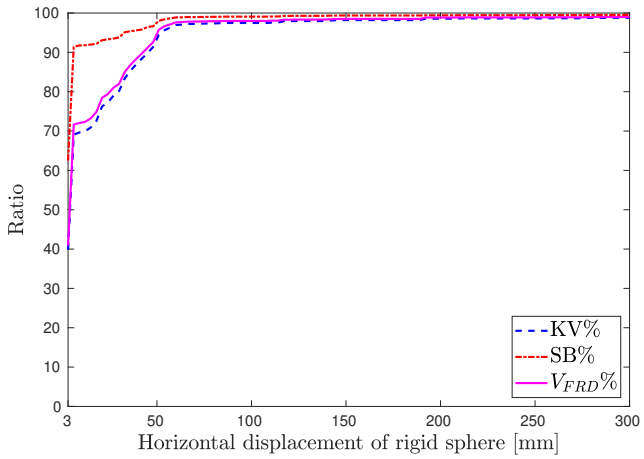

Figure 24: Details of the refinement with $\kappa_{\text{tol}} = 0.7$ and $V_{\text{tol}} = 5\,l_{uc}^3$ for the BCC lattice. The x axis starts from 3 mm because it is the first nonzero increment in the Newton incremental-iterative process.

savings can be expected and AGQC can allow simulating model sizes that are out of reach for DNS. The example also highlights the importance of *coarsening* in the wake of *refinement*, which is part of future work.

4.4 Scratching a Kelvin lattice with a rigid sphere

In this section, the scratching test of Section 4.3 is performed (same lattice size & boundary conditions) for a lattice comprised of Kelvin cells to illustrate that the proposed adaptive generalized QC method is applicable to any shape of cell as long as it is periodic. We also intend to demonstrate that for different types of lattices, the deformation can be substantially more local and that the QC framework therefore will result in different computational savings depending on the shape and therefore the stress transformation of the cell.

All the parameters of Section 4.3, except for κ_{tol} and V_{tol}, were preserved in the adaptive QC simulation. κ_{tol} is set to 1.3 and V_{tol} is set to $10\,l_{uc}^3$ (tuned by considering one increment corresponding to the simulation step size). Fig. 26

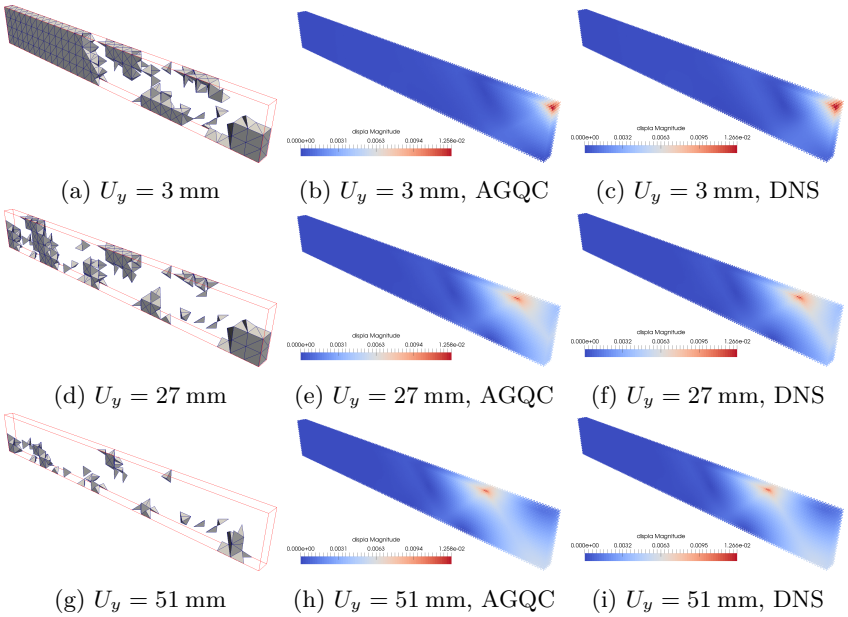

(a) $U_y = 3$ mm (b) $U_y = 3$ mm, AGQC (c) $U_y = 3$ mm, DNS

(d) $U_y = 27$ mm (e) $U_y = 27$ mm, AGQC (f) $U_y = 27$ mm, DNS

(g) $U_y = 51$ mm (h) $U_y = 51$ mm, AGQC (i) $U_y = 51$ mm, DNS

Figure 25: Results of the BCC lattice. Left column: the CGDs and the FRDs (void within the red outline) as a function of the displacement (U_y) of the rigid sphere. Middle column: contour of displacement magnitude (i.e. $\sqrt{U_x^2 + U_y^2 + U_z^2}$) of the lattice from adaptive QC simulation. Right column: contour of displacement magnitude of the lattice from the DNS.

plots the curves of the normal contact force versus the tangential displacement of the rigid sphere. Similar to Fig. 23, the force – displacement curve of Fig. 26 can be divided into three stages, i.e. the stage of contact establishment, the stage of "stable" contact regime and the stage of final loss of contact. A big difference between Fig. 23 and Fig. 26 is that for BCC cell, the transition between the stage of contact establishment and the stage of "stable" contact regime (also between the stage of "stable" contact regime and the stage of final loss of contact) is characterized by a drop (leap) of the contact force. For the Kelvin cell, the transition is relatively smooth. This can be explained by the more local response of Kelvin lattice attributed to the different layout of struts in the Kelvin cell. Kelvin cells have more diversified strut orientations compared to the BCC cell

and Kelvin lattice lacks long continuous diagonal strut.

The maximum contact force of the Kelvin cell is almost five times higher than that of the BCC cell and the magnitude of oscillation of the contact force of the Kelvin cell is also larger than that of the BCC cell. This can be explained by the effective density of the Kelvin cell being 2.08 times that of the BCC cell (computing the overall volume of all struts in a cell corresponding to the different cell topology).

Fig. 27 shows how KV%, SB% and V_{FRD}% (the volumetric fraction of the fully-resolved domains) change during the simulation for the Kelvin lattice. Compared to the BCC cell in Fig. 24, the refinement for the Kelvin cell is much more progressive. This can be explained by the fact that the response of the Kelvin cell is much more local compared to that of the BCC cell. This also means more efficient model reduction for cells that exhibit localized responses.

Fig. 28 plots the discretization of IPE & FRD and the displacement contours as a function of the location of the rigid sphere. Again, the proposed adaptive generalized QC method can successfully adapt the configuration of CGDs and FRDs during the simulation. The displacement contour also verifies the local deformation response of Kelvin cell.

Table 4 provides a detailed comparison between the model scale, the accuracy and the required computational time for the scratch tests of BCC lattice and Kelvin lattice. For both scratch tests, the AGQC simulations take longer time to finish compared to the DNS because of the iterations of refinement. It is noteworthy to point out that the simulation domains were chosen small enough to allow direct comparison with DNS, corresponding to model sizes disadvantageous for showing the performance gain of AGQC. As the Kelvin lattice yields a more localized response than the BCC lattice, the Kelvin lattice is progressively refined and resolved throughout the simulation and therefore results in a

more significant reduction of model scale (Fig. 24 and Fig. 27). It is also worth noting in Table 4 that the DNS simulations of the BCC lattice and the Kelvin lattice need quite different computational times. This is partially because each increment of the BCC lattice takes around three iterations to converge while each increment of the Kelvin lattice takes around five iterations to converge.

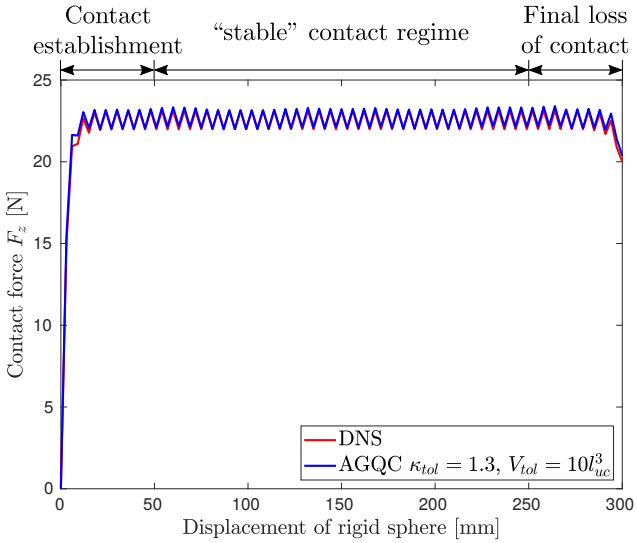

Figure 26: The contact force versus the displacement of the rigid sphere for DNS and AGQC approaches of the Kelvin lattice.

Cell shape	Model scheme	External work (N · mm)	Average number of DoFs	Average number of (sampling) beams	Average volume fraction of CGDs (%)	Computational time (hour)
BCC	DNS	1497.5	1,644,156	360,000	0	8.4
BCC	AGQC	+0.39%	-6.22%	-2.61%	5.63	+867.86%
Kelvin	DNS	6690.8	1,172,400	375,400	0	30.2
Kelvin	AGQC	+0.56%	-35.47%	-20.97%	35.55	+155.63%

Table 4: Comparison of model scale, accuracy and required computational time between the scratch tests of BCC lattice and Kelvin lattice. Only the percentage differences compared to the corresponding DNS are given for the QC simulations.

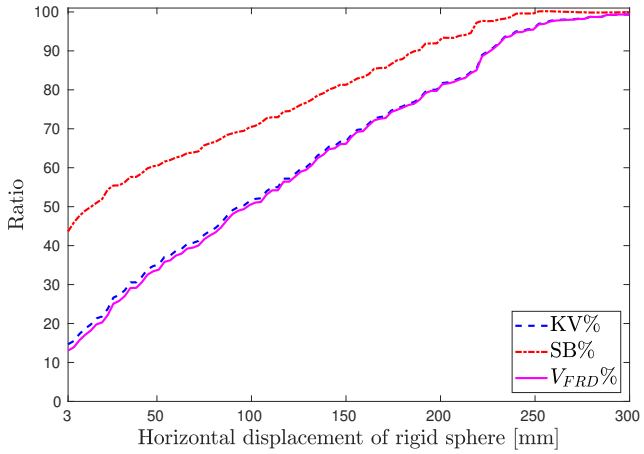

Figure 27: Details of the refinement with $\kappa_{\text{tol}} = 1.3$ and $V_{\text{tol}} = 10\, l_{uc}^3$ for the Kelvin lattice. The x axis starts from 3 mm because it is the first nonzero increment in the Newton incremental-iterative process.

4.5 Scratching a large Kelvin lattice with a rigid sphere

In this section, the scratching test of Section 4.4 is performed for a relatively large elastic Kelvin lattice. The lattice consists of $20 \times 150 \times 80$ Kelvin cells along the thickness, length and depth, respectively, resulting in a DNS model with 17,678,400 DoFs and 5,826,400 beam FEs. Such a simulation is no longer feasible by DNS in the current implementation because of the resulting system size but also because of the computational effort of the stiffness matrix assembly. This computational model size makes AGQC preferable to DNS. The boundary conditions were the same as in the previous scratch examples, to allow comparing results to Section 4.4, only the lattice size was increased. In the model of Section 4.4 the contact zone was already fully enveloped in the FRD. This, together with the local Kelvin lattice response, implies that a similar scratch response is expected for the larger lattice of this section.

The initial discretization of IPEs & FRD of the AGQC simulation is shown in Fig. 29. V_{tol} was set to $30\, l_{uc}^3$ and κ_{tol} to 1.5. Note that the parameters used

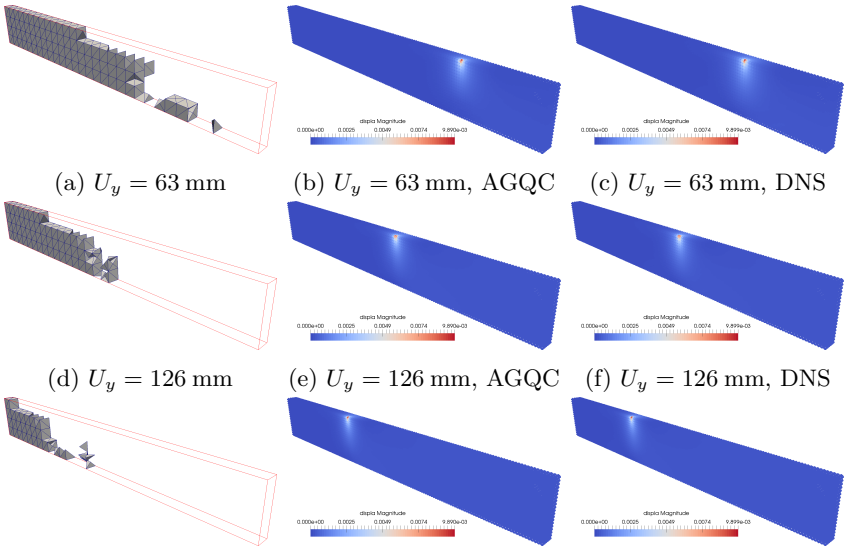

(a) $U_y = 63$ mm (b) $U_y = 63$ mm, AGQC (c) $U_y = 63$ mm, DNS

(d) $U_y = 126$ mm (e) $U_y = 126$ mm, AGQC (f) $U_y = 126$ mm, DNS

(g) $U_y = 189$ mm (h) $U_y = 189$ mm, AGQC (i) $U_y = 189$ mm, DNS

Figure 28: Results of the Kelvin lattice. Left column: the IPEs and the FRDs (void within the red outline) as a function of the displacement (U_y) of the rigid sphere. Middle column: contour of displacement magnitude (i.e. $\sqrt{U_x^2 + U_y^2 + U_z^2}$) of the lattice from adaptive QC simulation. Right column: contour of displacement magnitude of the lattice from the DNS.

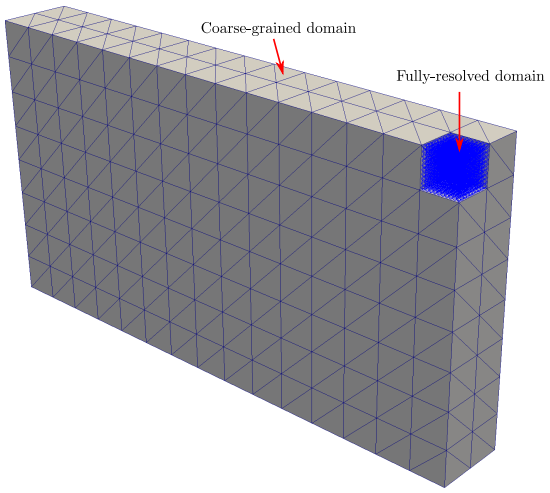

Figure 29: Initial discretization for the QC simulation of the Kelvin lattice. The refinement happens in all three spatial directions in comparison to Fig. 22.

in Section 4.4 [$\kappa_{\text{tol}} = 1.3$, $V_{\text{tol}} = 10\, l_{uc}^3$] were found to cause over-refining for this large Kelvin lattice while the force–displacement curves of the initial few increments remained almost identical with both sets.

Fig. 30 plots the curve of the normal contact force versus the tangential displacement of the rigid sphere from AGQC simulation. Note that the force–displacement curve of DNS in Section 4.4 is also incorporated in Fig. 30 for comparison, sharing a good match, as expected.

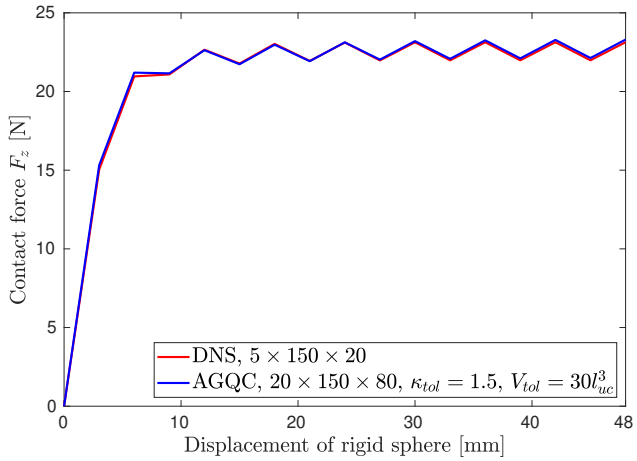

Figure 30: The normal contact force versus the tangential displacement of the rigid sphere for the large Kelvin lattice. Only a displacement of up to 48 mm is shown as the trend is apparent.

Fig. 31 illustrates the evolution of KV%, SB% and V_{FRD}% (the volumetric fraction of the fully-resolved domains) throughout the simulation. In comparison with Fig. 27, more significant model reduction is achieved, as expected, since this simulation operates in a model size domain in which QC type of approaches are intended and proved to be useful. Fig. 32 plots the discretization of IPEs & FRD as well as the corresponding displacement contour as a function of the location of the rigid sphere. Again, successful adaptation of the IPEs & FRD can be observed and, as opposed to the smaller example of Section 4.4,

this large model could also be used to tackle deeper scratch simulations with automatic adaptivity for a model size that would be prohibitive for DNS. It is pointed out that in Fig. 32 not the whole depth of the lattice is fully resolved compared to that of Fig. 28.

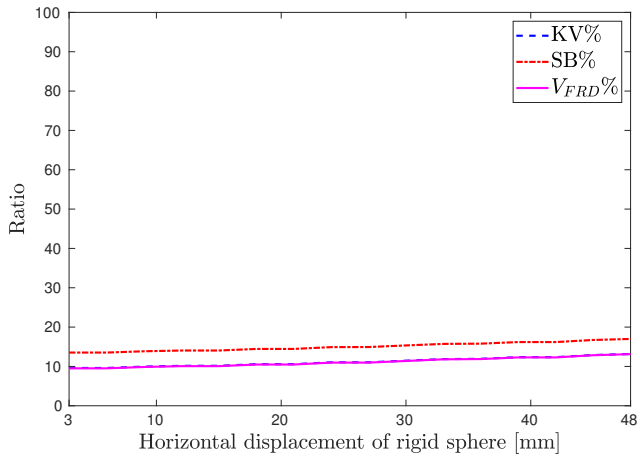

Figure 31: Details of the refinement with $\kappa_{\text{tol}} = 1.5$ and $V_{\text{tol}} = 30\, l_{uc}^3$ for the large Kelvin lattice. Only a displacement of up to 48 mm is shown as the trend is apparent. The x axis starts from 3 mm because it is the first nonzero increment in the Newton incremental-iterative process.

5 Conclusions

This work presented a refinement indicator for adaptive simulations of conventional and generalized quasicontinuum (QC) methods. The use of signaling cells between interpolation elements (IPEs) and at fully-resolved domains (FRDs) is a new idea that may yield new types of refinement indicators in the future. Our results show that the indicator does not trigger refinement in case of homogeneous deformations, rigid body translations and rigid body rotations (the latter being the result of the co-rotational beam formulation employed in the structural simulations).

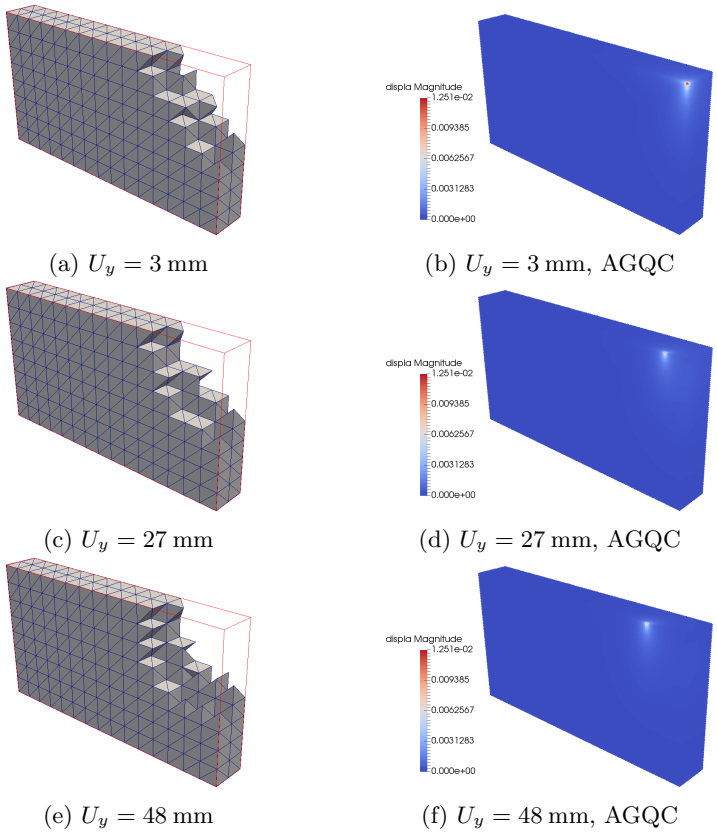

(a) $U_y = 3$ mm (b) $U_y = 3$ mm, AGQC

(c) $U_y = 27$ mm (d) $U_y = 27$ mm, AGQC

(e) $U_y = 48$ mm (f) $U_y = 48$ mm, AGQC

Figure 32: Results of the large Kelvin lattice. Left column: the IPEs and the FRDs (void within the red outline) as a function of the displacement (U_y) of the rigid sphere. Middle column: contour of displacement magnitude (i.e. $\sqrt{U_x^2 + U_y^2 + U_z^2}$) of the lattice from adaptive QC simulation.

The novel refinement indicator measures the discrepancy of the energy of signaling cells at interpolation element (IPE) surfaces (or edges in 2D). IPE refinement is triggered when the difference between the energies of a signaling cell reaches a user defined threshold, κ_{tol}. If the volume of a newly created IPE falls below a user defined minimum, V_{tol}, the IPE is transformed into a fully resolved domain (FRD). This prompts FRDs to both evolve and be created where necessary.

The examples revealed that the user defined threshold for [κ_{tol}, V_{tol}] have a

fundamental impact on the performance of the adaptive generalized QC method (AGQC) and a procedure for choosing them was proposed.

The proposed AGQC was applied to study BCC lattice and Kelvin lattices. The former showed a more nonlocal response while the latter exhibited a relatively local structured response. The difference was attributed to the distinct layouts and orientations of the struts in the cells. It was also shown that the local response of cells favors more significant model reduction when applying AGQC. By simulating two Kelvin lattices of different sizes, it was shown that AGQC is capable of tackling model sizes out of reach of DNS, keeping a satisfactory accuracy by employing an automatic adaptation of the spatial discretization (IPEs in CGDs and FRDs are updated on the fly). It was also demonstrated that the adaptivity parameters $[\kappa_{\text{tol}}, V_{\text{tol}}]$ are case specific and depend on the shape of the cell, the beam discretization of the cell and the size of the lattice.

Future work will focus on generalizing the indicator to incorporate dissipation (e.g. elastoplastic behavior). Since coarsening can further reduce the computational costs, a new coarsening indicator may also be formulated in the future.

6 Acknowledgment

Li Chen gratefully acknowledges the support of F.R.S.-FNRS (Belgium) under grant PDR No. 26033553 (EnLightenIt). Stéphane Bordas and Lars Beex gratefully acknowledge the financial support of the Fonds National de la Recherche Luxembourg FNRS-FNR grant INTER/FNRS/15/11019432/EnLightenIt/Bord as. Stéphane Bordas also gratefully acknowledges the support of the European Research Council Starting Independent Research Grant (ERC Stg grant agreement No. 279578) entitled "Towards real time multiscale simulation of cutting in non-linear materials with applications to surgical simulation and com-

puter guided surgery". Stéphane Bordas received funding from the European Union's Horizon 2020 research and innovation programme under grant agreement No 811099 TWINNING Project DRIVEN for the University of Luxembourg. The numerical simulations were carried out on the HPC platform Hydra co-operated by Université Libre de Bruxelles and Vrije Universiteit Brussel (see *https://hpc.vub.be/hydra.php*).

7 Data Availability Statement

The data that support the findings of this study are available from the corresponding author upon reasonable request.

References

[1] M. Arndt and M. Luskin. Error estimation and atomistic-continuum adaptivity for the quasicontinuum approximation of a frenkel–kontorova model. *Multiscale Modeling & Simulation*, 7(1):147–170, 2008.

[2] M. Arndt, V. Sorkin, and E.B. Tadmor. Efficient algorithms for discrete lattice calculations. *Journal of Computational Physics*, 228(13):4858 – 4880, 2009.

[3] J. M. Battini and C. Pacoste. Co-rotational beam elements with warping effects in instability problems. *Computer Methods in Applied Mechanics and Engineering*, 191(17):1755 – 1789, 2002.

[4] J. M. Battini and C. Pacoste. Plastic instability of beam structures using co-rotational elements. *Computer Methods in Applied Mechanics and Engineering*, 191(51):5811 – 5831, 2002.

[5] L. A. A. Beex, P. Kerfriden, T. Rabczuk, and S. P. A. Bordas. Quasicontinuum-based multiscale approaches for plate-like beam lattices experiencing in-plane and out-of-plane deformation. *Computer Methods in Applied Mechanics and Engineering*, 279:348 – 378, 2014.

[6] L. A. A. Beex, R. H. J. Peerlings, and M. G. D. Geers. A quasicontinuum methodology for multiscale analyses of discrete microstructural models. *International Journal for Numerical Methods in Engineering*, 87(7):701–718, 2011.

[7] L. A. A. Beex, R. H. J. Peerlings, and M. G. D. Geers. Central summation in the quasicontinuum method. *Journal of the Mechanics and Physics of Solids*, 70:242 – 261, 2014.

[8] L. A. A. Beex, R. H. J. Peerlings, and M. G. D. Geers. A multiscale quasicontinuum method for dissipative lattice models and discrete networks. *Journal of the Mechanics and Physics of Solids*, 64:154 – 169, 2014.

[9] L. A. A. Beex, R. H. J. Peerlings, and M. G. D. Geers. A multiscale quasicontinuum method for lattice models with bond failure and fiber sliding. *Computer Methods in Applied Mechanics and Engineering*, 269:108 – 122, 2014.

[10] L. A. A. Beex, R. H. J. Peerlings, K. van Os, and M. G. D. Geers. The mechanical reliability of an electronic textile investigated using the virtual-power-based quasicontinuum method. *Mechanics of Materials*, 80:52 – 66, 2015.

[11] L. A. A. Beex, O. Rokoš, J. Zeman, and S. P. A. Bordas. Higher-order quasicontinuum methods for elastic and dissipative lattice models: uniaxial deformation and pure bending. *GAMM-Mitteilungen*, 38(2):344–368, 2015.

[12] P. Z. Berke, R. H. J. Peerlings, T. J. Massart, and M. G. D. Geers. A homogenization-based quasi-discrete method for the fracture of heterogeneous materials. *Computational Mechanics*, 53(5):909–923, 2014.

[13] Li Chen, Lars A.A. Beex, Peter Z. Berke, Thierry J. Massart, and Stéphane P.A. Bordas. Generalized quasicontinuum modeling of metallic lattices with geometrical and material nonlinearity and variability. *Computer Methods in Applied Mechanics and Engineering*, 366:112878, 2020.

[14] M. Dobson, R. S. Elliott, M. Luskin, and E. B. Tadmor. A multilattice quasicontinuum for phase transforming materials: Cascading cauchy born kinematics. *Journal of Computer-Aided Materials Design*, 14(1):219–237, 2007.

[15] M. Dobson, M. Luskin, and C. Ortner. Stability, instability, and error of the force-based quasicontinuum approximation. *Archive for Rational Mechanics and Analysis*, 197(1):179–202, Jul 2010.

[16] D. Durville. Simulation of the mechanical behaviour of woven fabrics at the scale of fibers. *International Journal of Material Forming*, 3(2):1241–1251, Sep 2010.

[17] A. Gay Neto, P. M. Pimenta, and P. Wriggers. A master-surface to master-surface formulation for beam to beam contact. part i: frictionless interaction. *Computer Methods in Applied Mechanics and Engineering*, 303:400–429, may 2016.

[18] M.G.D. Geers, V.G. Kouznetsova, and W.A.M. Brekelmans. Multi-scale computational homogenization: Trends and challenges. *Journal of Computational and Applied Mathematics*, 234(7):2175 – 2182, 2010. Fourth International Conference on Advanced COmputational Methods in ENgineering (ACOMEN 2008).

[19] A. Ghareeb and A. Elbanna. An adaptive quasicontinuum approach for modeling fracture in networked materials: Application to modeling of polymer networks. *Journal of the Mechanics and Physics of Solids*, 137:103819, 2020.

[20] P. Kerfriden, J. J. Ródenas, and S. P. A. Bordas. Certification of projection-based reduced order modelling in computational homogenisation by the constitutive relation error. *International Journal for Numerical Methods in Engineering*, 97(6):395–422, 2014.

[21] J. Knap and M. Ortiz. An analysis of the quasicontinuum method. *Journal of the Mechanics and Physics of Solids*, 49(9):1899–1923, 2001. The JW Hutchinson and JR Rice 60th Anniversary Issue.

[22] D. M. Kochmann and J. S. Amelang. *The Quasicontinuum Method: Theory and Applications*, volume 245, chapter 8, pages 159–193. Springer International Publishing, Cham, Switzerland, 8 2016.

[23] D. M. Kochmann and G. N. Venturini. A meshless quasicontinuum method based on local maximum-entropy interpolation. *Modelling and Simulation in Materials Science and Engineering*, 22(3):034007, apr 2014.

[24] S. Kwon, Y. Lee, J. Y. Park, D. Sohn, J. H. Lim, and S. Im. An efficient three-dimensional adaptive quasicontinuum method using variable-node elements. *Journal of Computational Physics*, 228(13):4789 – 4810, 2009.

[25] J. Lengiewicz, J. Korelc, and S. Stupkiewicz. Automation of finite element formulations for large deformation contact problems. *International Journal for Numerical Methods in Engineering*, 85(10):n/a–n/a, aug 2010.

[26] M. Luskin and C. Ortner. An analysis of node-based cluster summation rules in the quasicontinuum method. *SIAM Journal on Numerical Analysis*, 47(4):3070–3086, 2009.

[27] M. Luskin, C. Ortner, and B. Van Koten. Formulation and optimization of the energy-based blended quasicontinuum method. *Computer Methods in Applied Mechanics and Engineering*, 253:160 – 168, 2013.

[28] M. Magliulo, A. Zilian, and L. A. A. Beex. Contact between shear-deformable beams with elliptical cross sections. *Acta Mechanica*, 231(1):273–291, 2020.

[29] T. J. Massart, R. H. J. Peerlings, and M. G. D. Geers. Structural damage analysis of masonry walls using computational homogenization. *International Journal of Damage Mechanics*, 16(2):199–226, 2007.

[30] A. Memarnahavandi, F. Larsson, and K. Runesson. A goal-oriented adaptive procedure for the quasi-continuum method with cluster approximation. *Computational Mechanics*, 55(4):617–642, Apr 2015.

[31] K. Mikeš and M. Jirásek. Quasicontinuum method combined with anisotropic microplane model. In *Modern Methods of Experimental and Computational Investigations in Area of Construction II*, volume 1144 of *Advanced Materials Research*, pages 142–147. Trans Tech Publications Ltd, 4 2017.

[32] K. Mikeš and M. Jirásek. Quasicontinuum simulation of nanotextile based on the microplane model. In *Proceedings of the 17th Conference on the Rehabilitation and Reconstruction of Buildings (CRRB 2015)*, volume 714 of *Key Engineering Materials*, pages 143–147. Trans Tech Publications Ltd, 11 2016.

[33] K. Mikeš and M. Jirásek. Quasicontinuum method extended to irregular lattices. *Computers & Structures*, 192:50 – 70, 2017.

[34] K. Mikeš, O. Rokoš, and R. H. J. Peerlings. Molecular statics simulation of nanoindentation using adaptive quasicontinuum method. In *Acta Polytechnica CTU Proceedings*, volume 15. Czech Technical University in Prague, 2018.

[35] R. Miller, M. Ortiz, R. Phillips, V. Shenoy, and E. B. Tadmor. Quasicontinuum models of fracture and plasticity. *Engineering Fracture Mechanics*, 61(3):427 – 444, 1998.

[36] R. E. Miller and E. B. Tadmor. The quasicontinuum method: Overview, applications and current directions. *Journal of Computer-Aided Materials Design*, 9(3):203–239, Oct 2002.

[37] C. Ortner and H. Wang. A priori error estimates for energy-based quasicontinuum approximations of a periodic chain. *Mathematical Models and Methods in Applied Sciences*, 21(12):2491–2521, 2011.

[38] G. P. Phlipot and D. M. Kochmann. A quasicontinuum theory for the nonlinear mechanical response of general periodic truss lattices. *Journal of the Mechanics and Physics of Solids*, 124:758 – 780, 2019.

[39] O. Rokoš, L. A. A. Beex, J. Zeman, and R. H. J. Peerlings. A variational formulation of dissipative quasicontinuum methods. *International Journal of Solids and Structures*, 102-103:214 – 229, 2016.

[40] O. Rokoš, R. H. J. Peerlings, and J. Zeman. eXtended variational quasicontinuum methodology for lattice networks with damage and crack propagation. *Computer Methods in Applied Mechanics and Engineering*, 320:769 – 792, 2017.

[41] O. Rokoš, R. H. J. Peerlings, J. Zeman, and L. A. A. Beex. An adaptive variational quasicontinuum methodology for lattice networks with localized damage. *International Journal for Numerical Methods in Engineering*, 112(2):174–200, 2017.

[42] M. Smith, Z. Guan, and W. J. Cantwell. Finite element modelling of the compressive response of lattice structures manufactured using the selective laser melting technique. *International Journal of Mechanical Sciences*, 67:28 – 41, 2013.

[43] J. P. Suárez, P. Abad, A. Plaza, and M. A. Padrón. Computational aspects of the refinement of 3d tetrahedral meshes. *Journal of Computational Methods in Sciences and Engineering*, 5(4):215–224, 2005.

[44] E. B. Tadmor, M. Ortiz, and R. Phillips. Quasicontinuum analysis of defects in solids. *Philosophical Magazine A*, 73(6):1529–1563, 1996.

[45] E. B. Tadmor, R. Phillips, and M. Ortiz. Mixed atomistic and continuum models of deformation in solids. *Langmuir*, 12(19):4529–4534, 1996.

[46] I. Tembhekar, J. S. Amelang, L. Munk, and D. M. Kochmann. Automatic adaptivity in the fully nonlocal quasicontinuum method for coarse-grained atomistic simulations. *International Journal for Numerical Methods in Engineering*, 110(9):878–900, 2017.

[47] B. Van Koten, X. H. Li, M. Luskin, and C. Ortner. *A Computational and Theoretical Investigation of the Accuracy of Quasicontinuum Methods*, pages 67–96. Springer Berlin Heidelberg, Berlin, Heidelberg, 2012.

[48] H. Wang. A posteriori error estimates for energy-based quasicontinuum approximations of a periodic chain, 2011.

[49] P. Wriggers. *Computational Contact Mechanics*. Springer Berlin Heidelberg, Berlin, Heidelberg, 2006.

[50] Y. Zhang and M. Gunzburger. Quadrature-rule type approximations to the quasicontinuum method for long-range interatomic interactions. *Computer Methods in Applied Mechanics and Engineering*, 199(9):648 – 659, 2010.